HHS Public Access

Author manuscript

Cell Rep. Author manuscript; available in PMC 2020 January 13.

Published in final edited form as:

Cell Rep. 2019 December 17; 29(12): 3885–3901.e5. doi:10.1016/j.celrep.2019.11.058.

Stasimon Contributes to the Loss of Sensory Synapses and Motor Neuron Death in a Mouse Model of Spinal Muscular Atrophy

Christian M. Simon[1,2,5,6], **Meaghan Van Alstyne**[1,2,6], **Francesco Lotti**[1,2], **Elena Bianchetti**[1,2], **Sarah Tisdale**[1,2], **D. Martin Watterson**[4], **George Z. Mentis**[1,2,3], **Livio Pellizzoni**[1,2,7,*]

[1]Center for Motor Neuron Biology and Disease, Columbia University, New York, NY 10032, USA

[2]Department of Pathology and Cell Biology, Columbia University, New York, NY 10032, USA

[3]Department of Neurology, Columbia University, New York, NY 10032, USA

[4]Department of Pharmacology, Northwestern University, Chicago, IL 60611, USA

[5]Present address: Carl-Ludwig-Institute for Physiology, Medical Faculty, University of Leipzig, Liebigstrasse 27, 04103 Leipzig, Germany

[6]These authors contributed equally

[7]Lead Contact

SUMMARY

Reduced expression of the survival motor neuron (SMN) protein causes the neurodegenerative disease spinal muscular atrophy (SMA). Here, we show that adeno-associated virus serotype 9 (AAV9)-mediated delivery of Stasimon—a gene encoding an endoplasmic reticulum (ER)-resident transmembrane protein regulated by SMN—improves motor function in a mouse model of SMA through multiple mechanisms. In proprioceptive neurons, Stasimon overexpression prevents the loss of afferent synapses on motor neurons and enhances sensory-motor neurotransmission. In motor neurons, Stasimon suppresses neurodegeneration by reducing phosphorylation of the tumor suppressor p53. Moreover, Stasimon deficiency converges on SMA-related mechanisms of p53 upregulation to induce phosphorylation of p53 through activation of p38 mitogen-activated protein kinase (MAPK), and pharmacological inhibition of this kinase prevents motor neuron death in SMA mice. These findings identify Stasimon dysfunction induced by SMN deficiency as an upstream driver of distinct cellular cascades that lead to synaptic loss and motor neuron degeneration, revealing a dual contribution of Stasimon to motor circuit pathology in SMA.

*Correspondence: lp2284@cumc.columbia.edu.

AUTHOR CONTRIBUTIONS

L.P. designed and supervised the study. C.M.S., M.V.A., F.L., E.B., and S.T. performed the experiments and analyzed the data. D.M.W. provided MW150 and advice on p38 MAPK inhibition. G.Z.M. contributed to the design, analysis, and interpretation of functional studies. C.M.S., M.V.A., and L.P. wrote the paper with input from all authors.

SUPPLEMENTAL INFORMATION

Supplemental Information can be found online at https://doi.org/10.1016/j.celrep.2019.11.058.

DECLARATION OF INTERESTS

The authors declare no competing interests.

Graphical Abstract

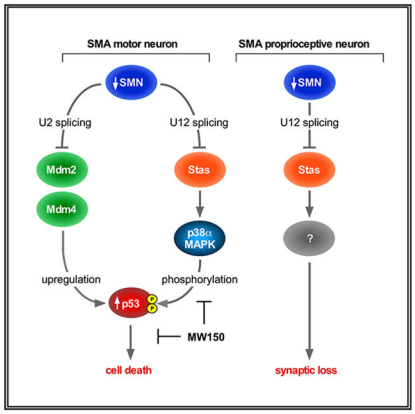

In Brief

SMN deficiency causes motor circuit dysfunction in SMA. Simon et al. show that Stasimon—an ER-resident protein regulated by SMN—contributes to sensory synaptic loss and motor neuron death in SMA mice through distinct mechanisms. In motor neurons, Stasimon dysfunction induces p38 MAPK-mediated phosphorylation of p53 whose inhibition prevents neurodegeneration.

INTRODUCTION

Spinal muscular atrophy (SMA) is an autosomal-recessive neuromuscular disorder characterized by the progressive loss of spinal motor neurons and skeletal muscle atrophy (Burghes and Beattie, 2009; Groen et al., 2018; Tisdale and Pellizzoni, 2015). SMA is a consequence of ubiquitous reduction in the levels of the survival motor neuron (SMN) protein because of homozygous deletion or mutation of the *SMN1* gene with retention of the hypomorphic *SMN2* gene (Lefebvre et al., 1995). SMN has a well-characterized role in the assembly of small nuclear ribonucleoproteins (snRNPs) of the splicing machinery (Meister et al., 2001; Pellizzoni et al., 2002) as well as the U7 snRNP, which functions in 3′ end processing of histone mRNAs (Pillai et al., 2003; Tisdale et al., 2013). SMN has also been implicated in other aspects of RNA regulation including mRNA transport (Donlin-Asp et al., 2017). Consistent with its central role in RNA processing (Donlin-Asp et al., 2016; Li et al., 2014), SMN deficiency has been shown to induce widespread splicing dysregulation and transcriptome alterations in a variety of *in vivo* models (Bäumer et al., 2009; Doktor et al., 2017; Jangi et al., 2017; Zhang et al., 2008, 2013). The identification of downstream RNA targets of SMN deficiency that directly contribute to SMA pathology is of critical importance for elucidating disease mechanisms and revealing SMN-independent therapeutic approaches. To date, however, this has proven to be challenging because of the diversity of RNA pathways controlled by SMN and the complexity of SMA pathology in mouse models that more closely resemble the most severe form of the human disease.

Motor neurons are the cell type most severely affected by SMN deficiency, and their degeneration is a hallmark of SMA pathology (Burghes and Beattie, 2009; Groen et al., 2018; Tisdale and Pellizzoni, 2015). Importantly, selective genetic restoration of SMN in

motor neurons of SMA mice has demonstrated that neuronal death is a cell autonomous process (Fletcher et al., 2017; Gogliotti et al., 2012; Martinez et al., 2012; McGovern et al., 2015), which could be exacerbated by non-autonomous contributions (Hua et al., 2015). We previously demonstrated that activation of the tumor suppressor p53 drives motor neuron degeneration in the SMNΔ7 mouse model of SMA (Simon et al., 2017). We also showed that selectivity is established through the convergence of distinct mechanisms of p53 regulation, including stabilization and phosphorylation of its N-terminal transactivation domain (TAD) (Simon et al., 2017), the latter of which occurs only in the pool of SMA motor neurons destined to die. Recently, we demonstrated that p53 upregulation results from dysregulated alternative splicing of Mdm2 and Mdm4–the two main inhibitors of p53 stability and function (Toledo and Wahl, 2006; Vousden and Prives, 2009)–because of reduced snRNP levels in SMA motor neurons (Van Alstyne et al., 2018a), directly linking neurodegeneration to specific splicing changes induced by SMN deficiency. However, the converging mechanism(s) responsible for selective phosphorylation of the TAD of p53 required for degeneration of SMA motor neurons is unknown.

Characterization of SMA pathogenesis has identified multiple synaptic deficits in the motor circuit beyond motor neuron death that include dysfunction as well as loss of neuromuscular junctions (NMJs) and central proprioceptive sensory synapses onto motor neurons (Shorrock et al., 2019; Van Alstyne and Pellizzoni, 2016), which likely exert compounding effects on neuromuscular function. Studies in mouse models indicated that NMJ denervation occurs as a consequence of intrinsic effects of SMN deficiency in SMA motor neurons, rather than skeletal muscle (Fletcher et al., 2017; Gavrilina et al., 2008; Iyer et al., 2015; Martinez et al., 2012), and that the pathogenic processes underlying NMJ denervation and death of motor neurons might be distinct (Kim et al., 2017; Van Alstyne et al., 2018a). The dysfunction and loss of proprioceptive synapses on somata and dendrites of SMA motor neurons are early pathogenic events in SMA mice (Mentis et al., 2011) and are caused by the effects of SMN deficiency within proprioceptive neurons (Fletcher et al., 2017). The resulting reduction of the excitatory drive from proprioceptive synapses induces membrane hyperexcitability and reduces the firing of motor neurons, contributing to impaired muscle contraction in SMA mice (Fletcher et al., 2017). Moreover, the deafferentation and dysfunction of motor neurons are mechanistically uncoupled from motor neuron death (Fletcher et al., 2017; Simon et al., 2016). However, although multiple insults to the synaptic integrity of sensory-motor circuits originate from defects in distinct neurons that coalesce to cause SMA pathology, the underlying SMN-dependent mechanisms are poorly understood.

This work aimed to address the outstanding questions described above by investigating the potential contribution of Stasimon dysfunction to SMA pathology in a mouse model of the disease. We previously identified Stasimon (also known as Tmem41b) as an evolutionarily conserved, U12 intron-containing gene regulated by SMN that is required for proper synaptic transmission in the motor circuit of *Drosophila* larvae and for motor axon outgrowth in zebrafish (Lotti et al., 2012). Importantly, Stasimon contributes to motor circuit deficits in *Drosophila* and zebrafish models of SMA because its overexpression suppresses specific neuronal phenotypes induced by SMN deficiency in those model organisms (Lotti et al., 2012). Furthermore, we and others have found that SMN deficiency disrupts U12 splicing (Boulisfane et al., 2011; Doktor et al., 2017; Jangi et al., 2017; Lotti et al., 2012),

and both misprocessing and reduced expression of Stasimon mRNA were found in disease-relevant motor circuit neurons of SMA mice (Lotti et al., 2012). Recent studies have also shown that Stasimon is a transmembrane protein localized to the endoplasmic reticulum (ER) that is essential for mouse embryonic development (Van Alstyne et al., 2018b) and is involved in autophagy (Moretti et al., 2018; Morita et al., 2018; Shoemaker et al., 2019). However, Stasimon's normal requirement in the mammalian motor circuit and a direct involvement in pathogenesis of SMA mouse models have not been established.

Here, we investigated the effects of Stasimon restoration in the SMNΔ7 mouse model of SMA by adeno-associated virus serotype 9 (AAV9)-mediated gene delivery. We found that overexpression of Stasimon rescues the loss of proprioceptive synapses on motor neurons, improves synaptic transmission, and suppresses motor neuron degeneration. Mechanistically, we demonstrate that the loss of Stasimon is sufficient to induce p53 phosphorylation–a key event underlying the selective degeneration of SMA motor neurons (Simon et al., 2017)–through stimulation of p38 mitogen-activated protein kinase (MAPK) signaling. Furthermore, pharmacological inhibition of p38 MAPK selectively suppresses p53 phosphorylation and motor neuron death in SMA mice. Together, these results establish Stasimon's direct involvement in distinct pathogenic cascades induced by SMN deficiency in proprioceptive neurons and motor neurons, revealing a dual contribution by Stasimon to sensory-motor circuit dysfunction in a mouse model of SMA. They also suggest that p38 MAPK inhibition might be a neuroprotective approach for combinatorial treatment of SMA together with SMN-inducing drugs.

RESULTS

AAV9-Mediated Stasimon Gene Delivery Improves Motor Function in SMA Mice

We investigated the effects of increased expression of human Stasimon (STAS) on the phenotype of SMNΔ7 SMA mice by intracerebroventricular (i.c.v.) injection of self-complementary AAV9 vectors at post-natal day zero (P0), an established method to study SMA disease mechanisms *in vivo* (Passini et al., 2010; Robbins et al., 2014; Simon et al., 2017; Van Alstyne et al., 2018a). qRT-PCR analysis confirmed that injection of AAV9-STAS, as well as AAV9-GFP and AAV9-SMN, which were used as negative and positive controls, respectively, resulted in robust expression of the corresponding mRNAs in the spinal cord of SMA mice at P11 (Figures 1A and S1A). AAV9-STAS did not increase full-length SMN2 mRNA or SMN protein levels in the spinal cords of SMA mice (Figures 1A and 1B). To rule out any potential indirect effects of AAV9-STAS on SMN function, we also looked at representative downstream targets of SMN-regulated RNA pathways. AAV9-STAS did not correct aberrant U12 splicing of endogenous Stasimon pre-mRNA (Lotti et al., 2012) or other RNA processing events, such as U7-dependent histone H1c 3′ end misprocessing (Tisdale et al., 2013), p53-dependent induction of Cdkn1a mRNA (Simon et al., 2017; Van Alstyne et al., 2018a), and reduced Chodl mRNA expression (Bäumer et al., 2009; Zhang et al., 2008) in the spinal cords of SMA mice at P11 (Figure S1B). In contrast, all of these SMN-dependent events were robustly corrected by AAV9-SMN, as expected (Figure S1B). Consistent with Stasimon being a downstream mRNA target of U12 splicing dysfunction

induced by SMN deficiency (Lotti et al., 2012), these results demonstrate that AAV9-STAS does not enhance SMN expression or function.

We next investigated the effects of AAV9-STAS on the disease phenotype of SMNΔ7 SMA mice (Le et al., 2005), which exhibit reduced weight, shortened lifespan, and impaired motor behavior. Wild-type (WT) mice injected with AAV9-STAS showed no phenotypic abnormalities relative to uninjected WT littermates (Figures 1C, S1C, and S1D), indicating no toxic effects of Stasimon overexpression during postnatal mouse development. Furthermore, AAV9-SMN corrected all behavioral parameters and robustly extended survival in SMA (Figures S1C and S1D), as previously described (Foust et al., 2010; Passini et al., 2010). Remarkably, although AAV9-STAS had no effects on weight gain and survival, it improved motor behavior in SMA mice, as assessed by righting time (Figure 1C). Thus, Stasimon contributes to the motor phenotype of SMA mice, and the functional improvement elicited by AAV9-STAS occurs independent of SMN upregulation.

AAV9-STAS Rescues the Loss of Proprioceptive Synapses on SMA Motor Neurons

To identify morphological improvements underlying the motor benefit of Stasimon restoration in SMA mice, we focused on synaptic connectivity of sensory-motor circuits controlling disease-relevant axial muscles. First, we analyzed the number of proprioceptive synapses onto motor neurons in the L1 lumbar spinal segment, which are strongly reduced in SMA mice (Mentis et al., 2011). To do so, we used immunohistochemistry with antibodies against the vesicular glutamate transporter 1 (VGluT1) to label proprioceptive synapses and choline acetyltransferase (ChAT) as a motor neuron marker. SMA mice injected with AAV9-GFP exhibited a strong reduction in proprioceptive synapses onto somata and dendrites of L1 motor neurons at P11, relative to WT mice (Figures 1D, 1F, and 1G). Strikingly, AAV9-STAS rescued the numbers of proprioceptive inputs on the somata and dendrites of motor neurons in SMA mice to levels similar to that of AAV9-SMN (Figures 1D, 1F, and 1G).

To examine the selectivity of Stasimon's effects on synaptic loss, we investigated NMJ innervation of the quadratus lumborum (QL), a disease-relevant axial muscle innervated by vulnerable L1-L3 motor neurons, which is severely denervated in SMA mice (Fletcher et al., 2017; Simon et al., 2017; Van Alstyne et al., 2018a). To do so, we used antibodies against neurofilament (NF-M) and synaptophysin (SYP) as presynaptic markers and fluorescently labeled α-bungarotoxin (BTX) to label the acetylcholine receptor clusters on muscle fibers. At P11, NMJs of the QL in SMA animals injected with AAV9-GFP display ~40% denervation, in contrast to being fully innervated in WT mice (Figures 1E and 1H). Moreover, although AAV9-SMN injection restored NMJ innervation of the QL to near-normal levels, AAV9-STAS did not have any effect on NMJ denervation in SMA mice (Figures 1E and 1H).

Taken together, these results reveal that Stasimon selectively restores the number of proprioceptive synapses in the sensory-motor circuit of SMA mice.

Stasimon Acts in Proprioceptive Neurons to Improve Sensory-Motor Synaptic Transmission in SMA Mice

We sought to determine whether restoration of proprioceptive synapses on SMA motor neurons by AAV9-STAS resulted in functional improvement of sensory-motor neurotransmission, which is severely disrupted in SMA mice (Fletcher et al., 2017; Mentis et al., 2011). To do so, we used the spinal cord *ex vivo* preparation and determined the amplitude of the sensory-motor monosynaptic reflex in the L1 spinal segment by simultaneous stimulation of the L1 dorsal root and recording from the homonymous ventral root of WT and SMA mice at P11 (Mentis et al., 2011). The amplitude of the monosynaptic reflex was reduced by ~95% in SMA mice injected with AAV9-GFP and robustly enhanced upon SMN restoration with AAV9-SMN (Figures 2A and 2B). When we analyzed SMA mice injected with AAV9-STAS, we identified two distinct physiological responses in approximately equal proportions: a group of AAV9-STAS mice that exhibited a robust improvement of the monosynaptic reflex comparable to that of AAV9-SMN-injected SMA mice (Figures 2A, 2B, and S2A), and another group that did not show increased response relative to AAV9-GFP-treated SMA mice (Figure S2A). There were no significant differences between the two groups of SMA mice treated with AAV9-STAS in their body weight (Figure S2B), the levels of viral-mediated STAS mRNA overexpression in the spinal cord (Figure S2C), or the number of proprioceptive synapses on SMA motor neurons (aggregated data are shown in Figures 1F and 1G) that could account for this observation. However, there was correlation with the motor performance of these SMA mice. We found that AAV9-STAS (R, righting) treated SMA mice that were able to right at the time of the assay (Figure S2D) had robust spinal reflex amplitudes (Figures 2A, 2B, and S2A), whereas AAV9-STAS (NR, non-righting) SMA mice with poor righting ability (Figure S2D) had small amplitudes (Figure S2A). Moreover, the levels of exon 7 containing, full-length SMN2 mRNA were greater in the spinal cord of AAV9-STAS (R) relative to AAV9-STAS (NR) SMA mice (Figure S2E). A marked reduction of SMN2 exon 7 splicing ensues at late symptomatic stages in SMA mice because of hypoxia and malnourishment, which exacerbate disease progression (Bebee et al., 2012; Sahashi et al., 2012), likely by enhancing a negative feedback loop that suppresses exon 7 splicing (Jodelka et al., 2010; Ruggiu et al., 2012). Thus, the observed differences in the electrophysiological responses of AAV9-STAS-treated mice might reflect a degree of heterogeneity in the underlying severity of the SMA phenotype. Nevertheless, these experiments suggest that AAV9-STAS-mediated restoration of proprioceptive synapses can result in functional improvement of sensory-motor neurotransmission that correlates with enhanced motor function in SMA mice.

We next investigated NMJ function by stimulating motor axons in the L1 ventral root and recording the resultant compound muscle action potential (CMAP) in the QL muscle at P11. The CMAP of SMA mice injected with AAV9-GFP was strongly reduced compared with that of WT mice and was significantly improved by AAV9-SMN injection (Figures 2C and 2D). AAV9-STAS-injected SMA mice did not show any improvement in the CMAP (Figures 2C and 2D), which was the case irrespective of their motor behavior or spinal reflex amplitudes at the time of the assay (Figure S2F) and is consistent with the lack of effects on NMJ innervation (Figures 1E and 1H). Thus, the effects of Stasimon are selective for proprioceptive sensory synapses in SMA mice.

To further dissect the Stasimon-dependent functional improvement of the sensory motor circuit, we first determined the cellular contribution of motor neurons and proprioceptive synapses to the amplitude of the monosynaptic reflex in SMA mice. To do so, we restored SMN selectively in either proprioceptive neurons (SMA+SMN [PV-Cre]) or motor neurons (SMA+SMN [ChAT-Cre]) of SMA mice using a conditional allele for Cre-dependent SMN restoration (Lutz et al., 2011). We have previously demonstrated that this approach rescues the number and function of proprioceptive neurons in SMA+SMN (PV-Cre) mice and motor neuron survival in SMA+SMN (ChAT-Cre) mice, respectively (Fletcher et al., 2017). Here, we found that motor neurons and proprioceptive neurons equally contribute to the reduction in the amplitude of the monosynaptic reflex of SMA mice (Figures S2G and S2H). To determine the reliability of neurotransmission of proprioceptive synapses irrespective of the number of motor neurons present, we performed repetitive stimulation of the sensory dorsal root L1 with simultaneous recording of the ventral root at high frequency (10 Hz) and compared the monosynaptic amplitude of the first with the fifth stimulus, as in previous studies (Fletcher et al., 2017; Simon et al., 2017). The ventral root amplitude after a single stimulus is the result of motor neuron activation and depends on the number and function of proprioceptive synapses and the number of motor neurons present. However, at higher stimulation frequencies (10 Hz), the ventral root amplitude change depends only on the function of proprioceptive synapses because the number of synapses and the number of motor neurons are the same for the different sequential stimuli. We found a decrease in the monosynaptic amplitude from the first and fifth stimulus of ~40% in WT and ~70% in SMA mice (Figures 2E and 2F), revealing greater synaptic depression in SMA mice, which is likely due to impaired neurotransmission. Although selective SMN restoration in motor neurons of SMA+SMN (ChAT-Cre) mice did not have any benefit, SMN expression in proprioceptive neurons of SMA+SMN (PV-Cre) mice reduced the synaptic depression of the monosynaptic reflex to WT levels (Figures 2E and 2F), confirming that this experimental approach distinguishes the presynaptic contribution of proprioceptive neurotransmission in SMA. Importantly, SMA mice injected with AAV9-STAS showed a correction of synaptic depression to levels comparable to that of WT and AAV9-SMN-treated SMA mice (Figures 2G and 2H). Collectively, these results indicate that AAV9-STAS ameliorates SMN-dependent sensory-motor circuit deficits, at least in part, by improving synaptic transmission in proprioceptive neurons of SMA mice.

Stasimon Contributes to Motor Neuron Degeneration in SMA Mice

Loss of motor neurons is a hallmark of SMA pathology (Burghes and Beattie, 2009; Groen et al., 2018; Tisdale and Pellizzoni, 2015), and we investigated whether Stasimon was implicated in this neurodegenerative process. To do so, we performed immunohistochemistry experiments and visualized motor neurons in the L1 and L5 spinal segments with antibodies against ChAT (Figures 3A and 3C). SMA mice injected with AAV-GFP displayed a loss of vulnerable L1 and L5 medial motor column (MMC) motor neurons at P11 (Figures 3B and 3D). Importantly, AAV9-STAS corrected that loss of SMA motor neurons with an efficacy similar to AAV9-SMN (Figures 3B and 3D). We recently showed that motor neuron death is caused by distinct, converging mechanisms of p53 activation in the SMNΔ7 mouse model (Simon et al., 2017; Van Alstyne et al., 2018a). To investigate whether Stasimon suppresses motor neuron death through the p53 pathway, we first

immunostained against p53 and found no effects of AAV9-STAS on the number of $p53^{+}$ L5 MMC motor neurons relative to AAV9-GFP-treated SMA mice (Figures 4A and 4B), consistent with p53 upregulation being dependent on dysregulation of Mdm2 and Mdm4 alternative splicing (Van Alstyne et al., 2018a). Death of SMA motor neurons requires at least one other event converging on p53 that includes, but is not limited to, phosphorylation of p53 serine 18 (Simon et al., 2017)–a selective marker of degenerating SMA motor neurons. We found that AAV9-STAS significantly reduced the percentage of vulnerable L5 MMC motor neurons expressing phosphorylated $p53^{S18}$ ($p\text{-}p53^{S18}$) in SMA (Figures 4C and 4D), consistent with Stasimon overexpression preventing SMA motor neuron death through modulation of p53 phosphorylation. Altogether, these experiments place Stasimon dysfunction upstream of the cascade of events driving phosphorylation of p53 and the subsequent process of motor neuron degeneration in SMA mice.

Stasimon Deficiency Is Sufficient to Induce $p53^{S18}$ Phosphorylation

Recent studies have shown that Stasimon is required for autophagy in cultured mammalian cells (Moretti et al., 2018; Morita et al., 2018; Shoemaker et al., 2019). There have also been reports of autophagy dysregulation in SMA (Custer and Androphy, 2014; Gonçalves et al., 2018; Periyakaruppiah et al., 2016; Piras et al., 2017; Rodriguez-Muela et al., 2018). Therefore, we sought to investigate the possible involvement of Stasimon-dependent autophagy defects in SMA pathogenesis. First, we established a stable NIH 3T3 cell line (NIH 3T3-$Stas_{RNAi}$) in which Stasimon mRNA levels are reduced by RNAi to ~10% of normal as monitored by qRT-PCR (Figure S3A). We then analyzed by western blot the levels of the autophagy proteins p62 and LC3 in WT and $Stas_{RNAi}$ NIH 3T3 cells under basal conditions and after autophagy induction with serum starvation or inhibition by bafilomycin A1 treatment (Figure S3B). We found that the levels of p62 and lipidated LC3 (LC3-II) were moderately increased in Stasimon-deficient relative to WT cells, which is consistent with dysregulation of autophagy (Moretti et al., 2018; Morita et al., 2018; Shoemaker et al., 2019). However, western blot analysis showed no changes in the levels of either p62 and LC3 in spinal cords from WT and SMA mice at P6 and P11 (Figures S3C and S3D). Additionally, we performed immunohistochemistry experiments to investigate p62 expression in L1 motor neurons and proprioceptive neurons from L1 dorsal root ganglia (DRGs) of WT and SMA mice (Figures S3E and S3F) but did not find any major difference in the levels and localization of p62 induced by SMN deficiency in these disease-relevant neurons *in vivo*. These results suggest that autophagy dysregulation is unlikely to underlie the Stasimon-dependent deficits in the SMA motor circuit.

Next, we sought to determine whether loss of Stasimon is sufficient to induce $p53^{S18}$ phosphorylation as suggested by the reduction of $p\text{-}p53^{S18}$ in SMA motor neurons described above. We have previously shown that upregulation, but not N-terminal phosphorylation, of p53 in SMA motor neurons is due to dysregulation of Mdm2 and Mdm4 alternative splicing (Van Alstyne et al., 2018a). Therefore, we devised a cell-based assay to investigate the role of Stasimon deficiency on $p53^{S18}$ phosphorylation after p53 anti-repression induced by modulation of Mdm2 and Mdm4 splicing (Figure 4E). To do so, we treated WT and $Stas_{RNAi}$ NIH 3T3 cells with either control morpholino oligonucleotides (MOs) or with splice-switching MOs that induce selective skipping of Mdm2 exon 3 and Mdm4 exon 7

(Figure 4F), as previously reported (Van Alstyne et al., 2018a). We then performed immunofluorescence analysis and determined the percentage of treated NIH 3T3 cells with nuclear accumulation of either p53 or p-p53^{S18}. Treatment with Mdm2/4 MOs induced strong stabilization and nuclear accumulation of p53 in nearly all WT and Stas$_{RNAi}$ NIH 3T3 cells (Figures 4G and 4H), whereas there was no detectable nuclear p53 in cells treated with control MO. Importantly, we found that p53^{S18} was phosphorylated in nearly 80% of Stas$_{RNAi}$ NIH 3T3 cells treated with Mdm2/4 MOs (Figures 4I and 4J), whereas little, if any, p-p53^{S18} was detected in any other treatment groups. These results show that Stasimon deficiency does not induce stabilization and nuclear accumulation of p53 in mammalian cells; however, loss of Stasimon is sufficient to induce N-terminal phosphorylation of p53 when converging with pre-existing mechanisms of p53 upregulation, mechanistically paralleling the paradigm driving degeneration of motor neurons in the SMA mouse model.

Stasimon-Dependent p53^{S18} Phosphorylation Is Mediated by p38 MAPK

SMN deficiency has been shown to activate several kinases (Wu et al., 2011; Genabai et al., 2015; Kannan et al., 2018; Miller et al., 2015; Ng et al., 2015), including p38 MAPK, which directly phosphorylates serine 18 of p53 (Toledo and Wahl, 2006; Vousden and Prives, 2009). We also found that pharmacological inhibition of p38 MAPK in SMA mice enhances motor function without increasing SMN expression (D.M.W and L.P., unpublished data). Therefore, to gain insight into the mechanisms of Stasimon-mediated p53 phosphorylation, we investigated the potential involvement of the p38 MAPK pathway. First, we analyzed the effects of MW150–a highly selective inhibitor of the α isoform of p38 MAPK (Roy et al., 2015; Watterson et al., 2013)–on phosphorylation of p53 induced by Stasimon deficiency in our cell-based model system (Figure 4E). To do so, NIH 3T3-Stas$_{RNAi}$ cells were cultured in the presence of vehicle (saline) or MW150 before the addition of control and Mdm2/4 MOs, followed by analysis of p53 expression and p53^{S18} phosphorylation by immunocytochemistry. Remarkably, although MW150 treatment did not affect the induction of p53 by Mdm2/4 MOs (Figures 5A and 5B), it strongly suppressed the levels of p53^{S18} phosphorylation (Figures 5C and 5D). Furthermore, Stasimon deficiency stimulated p38 MAPK activation in NIH 3T3 cells, as indicated by increased levels and nuclear accumulation of p38 MAPK phosphorylated at threonine 180 and tyrosine 182 (Figure S4) (Plotnikov et al., 2011). These results indicate that Stasimon deficiency induces p53^{S18} phosphorylation through activation of p38α MAPK signaling.

Next, we investigated whether p38α MAPK activation contributes to p53^{S18} phosphorylation in SMA motor neurons by taking advantage of the established permeability of MW150 (Roy et al., 2019) in the CNS. We treated SMA mice daily by intraperitoneal (i.p.) injection with either saline or 5 mg/kg of MW150–a dose previously demonstrated to effectively inhibit p38α MAPK in the CNS and to improve the phenotype of mouse models of neurological disease (Robson et al., 2018; Roy et al., 2015, 2019; Rutigliano et al., 2018; Zhou et al., 2017). Importantly, MW150 treatment robustly decreased the levels of p53^{S18} phosphorylation but not the induction of p53 in vulnerable L5 MMC SMA motor neurons relative to vehicle-treated SMA mice at P11 (Figures 5E–5H), directly linking p38α MAPK activation to the phosphorylation of p53^{S18} in SMA motor neurons.

Pharmacological Inhibition of p38 MAPK Prevents Degeneration of SMA Motor Neurons

We reasoned that p38α MAPK inhibition might have neuroprotective effects in SMA mice based on the suppression of p53 phosphorylation observed with MW150 treatment. To test that possibility, we treated SMA mice with daily i.p. injections of vehicle or MW150 (5 mg/kg) and then determined the number of motor neurons, relative to untreated WT mice, at P11 by immunohistochemistry with anti-ChAT antibodies. Remarkably, we found that MW150 treatment was able to suppress the death of vulnerable L1 and L5 MMC motor neurons in SMA mice (Figures 6A–6D). We also tested the effects of MW150 treatment on the number of $VGluT1^{+}$ proprioceptive synapses on L1 motor neurons (Figures 6E and 6F) as well as on the percentage of NMJ innervation in the vulnerable QL muscle (Figures 6G and 6H). However, we found no evidence for correction of either of these synaptic deficits in SMA mice treated with MW150 relative to vehicle-treated SMA mice. Together these results reveal a direct pathogenic contribution of p38α MAPK activation to p53-mediated motor neuron death and the robust neuroprotective effects of MW150 treatment in a mouse model of SMA.

DISCUSSION

Motor dysfunction in SMA involves integration of multiple pathogenic insults induced by SMN deficiency in distinct neurons of the motor circuit (Shorrock et al., 2019; Van Alstyne and Pellizzoni, 2016). SMN has key functions in several RNA pathways that control gene expression (Donlin-Asp et al., 2016; Li et al., 2014) and establishing causal links between dysregulation of downstream mRNA targets of SMN and SMA pathogenesis is fundamental to understanding disease mechanisms as well as to identifying genes and pathways relevant for sensory-motor function that may also represent therapeutic targets. Here, we show that AAV9-mediated Stasimon gene delivery improves motor function and corrects select pathogenic events in the motor circuit of SMA mice. Stasimon overexpression prevents the loss of proprioceptive synapses on somata and dendrites of SMA motor neurons with consequent functional improvement of sensory-motor neurotransmission that correlates with improved motor function. Stasimon restoration also rescues vulnerable SMA motor neurons from degeneration, which we have previously shown to involve distinct mechanisms of p53 activation, including both upregulation and phosphorylation of the N-terminal TAD of p53 (Simon et al., 2017). Importantly, our results indicate that Stasimon dysfunction induced by SMN deficiency triggers a p38 MAPK-dependent signaling cascade that drives p53 phosphorylation and motor neuron death in SMA mice. Taken together, these findings reveal the direct contribution of Stasimon to distinct deficits in the sensory-motor circuit of SMA mice. They also highlight an unexpected link of Stasimon dysfunction with p38 MAPK activation and p53-dependent mechanisms of neurodegeneration as well as a potential pharmacological approach for neuroprotection in SMA.

Our findings that Stasimon restoration improves some, but not all, of the disease-related deficits in SMA mice support the view that a composite set of defects involving SMN-dependent RNA splicing alterations in specific genes and possibly disruption of other RNA pathways contribute to SMA pathology. We previously discovered Stasimon as a U12-intron containing gene regulated by SMN whose dysfunction results in specific neuronal deficits in

the motor circuit of *Drosophila* and zebrafish models of SMA (Lotti et al., 2012). Here, we reveal the contribution of Stasimon to SMA pathology in a mouse model that more accurately recapitulates genetic and phenotypic aspects of the human disease, establishing Stasimon as a disease-relevant target of SMN deficiency across evolution. Furthermore, because Stasimon expression is affected by U12 splicing dysfunction induced by SMN deficiency (Doktor et al., 2017; Lotti et al., 2012), this study strengthens the proposed pathogenic role of minor splicing disruption and the identification of Stasimon as an effector of U12-dependent motor circuit deficits in SMA, expanding our understanding of the RNA-mediated mechanisms of the disease.

Based on our findings and earlier genetic studies in SMA mice, it is plausible to draw conclusions with regard to the spatial contribution of Stasimon to motor circuit pathology (Figure 7). On one hand, selective restoration of SMN in motor neurons indicated that induction of p53 (Simon et al., 2017) and cell death Fletcher et al., 2017; Gogliotti et al., 2012; Martinez et al., 2012; McGovern et al., 2015) are cell autonomous, suggesting that the effects of AAV9-STAS on SMA motor neuron survival are mediated by Stasimon restoration in these cells. Consistent with this conclusion, both AAV9-STAS and p38 MAPK inhibition suppress p53 phosphorylation in SMA motor neurons. On the other hand, deafferentation is caused by the effects of SMN deficiency in proprioceptive neurons (Fletcher et al., 2017), and our results directly implicate Stasimon dysfunction in this process. Importantly, our findings that the loss of sensory synapses is independent of p53 (Van Alstyne et al., 2018a; Simon et al., 2017) and that p38 MAPK inhibition does not improve deafferentation in SMA mice point to distinct pathogenic cascades downstream of Stasimon dysfunction in motor neurons and proprioceptive neurons. In agreement with the spatial requirement of SMN and Stasimon in the *Drosophila* motor circuit (Imlach et al., 2012; Lotti et al., 2012), our studies of synaptic depression further indicate that Stasimon acts in proprioceptive neurons to improve the function of sensory-motor synapses. Given that silencing proprioceptive neurotransmission alone does not induce synaptic loss (Fletcher et al., 2017; Mendelsohn et al., 2015), it is possible that synaptic dysfunction and deafferentation will result from the disruption of distinct Stasimon-dependent events within proprioceptive neurons. Additional mechanistic studies are required to determine the specific cellular defects induced by Stasimon dysfunction that lead to impaired synaptic transmission and deafferentation. These events are also different from those underlying the loss of NMJ synapses as indicated by the lack of improvement in neuromuscular innervation by Stasimon overexpression in SMA mice. Lastly, consistent with previous studies (Kim et al., 2017; Van Alstyne et al., 2018a), the protective effect of Stasimon on motor neuron survival, but not NMJ innervation, supports the view that these pathogenic hallmarks of SMA, although both originating in motor neurons, are mechanistically uncoupled.

Based on previous studies in the SMNΔ7 mouse model of SMA (Simon et al., 2017), we have proposed a model in which selective degeneration of vulnerable SMA motor neurons requires the convergence of p53 stabilization with one or more additional events, which include post-translational modifications of p53 such as phosphorylation of its N-terminal TAD that specifically direct the p53 response toward degeneration (Figure 7). We recently demonstrated that dysregulation of Mdm2 and Mdm4 alternative splicing induced by SMN deficiency underlies the upregulation, but not the phosphorylation, of p53 in SMA motor

neurons (Van Alstyne et al., 2018a). Consistent with the proposed model, we also showed that these splicing events are necessary but not sufficient to induce motor neuron death *in vivo* (Van Alstyne et al., 2018a), leaving open the question as to which downstream targets of SMN are involved in p53 phosphorylation. Our findings that AAV9-STAS and p38 MAPK inhibition reduces phosphorylation of $p53^{S18}$ and rescues survival of SMA motor neurons *in vivo*, together with the observation that Stasimon deficiency is sufficient to induce p38 MAPK-mediated $p53^{S18}$ phosphorylation *in vitro*, fill this knowledge gap, placing Stasimon dysfunction upstream of a p38 MAPK/p53-dependent neurodegenerative axis (Figure 7).

SMN deficiency induces the activation of several kinases that have been implicated in the degeneration of SMA motor neurons (Genabai et al., 2015; Kannan et al., 2018; Miller et al., 2015; Ng et al., 2015) and are known to phosphorylate p53 (Toledo and Wahl, 2006; Vousden and Prives, 2009), including the stress-activated protein kinases JNK and p38 MAPK (Genabai et al., 2015; Wu et al., 2011). It was recently suggested that loss of (SMA motor neurons is not associated with JNK/c-Jun signaling (Pilato et al., 2019). Here, leveraging on the availability of MW150–a highly selective, CNS-permeable inhibitor of p38α MAPK (Roy et al., 2015)–we implicate a direct pathogenic contribution of p38 MAPK activation to p53-mediated motor neuron death in SMA mice. Furthermore, degeneration of SMA motor neurons requires phosphorylation of the N-terminal TAD of mouse p53 at multiple residues beyond serine 18 (Simon et al., 2017), including serines 37 and 58 (corresponding to serines 33 and 46 of human p53), which are known to be phosphorylated by p38 MAPK (Toledo and Wahl, 2006). Although our data do not distinguish whether p38 MAPK phosphorylates p53 directly or through downstream kinases in SMA motor neurons, Stasimon dysfunction and p38 MAPK activation likely trigger some of these additional p53 modifications required for neurodegeneration, but the lack of specific reagents prevents further analysis at this time. Future studies are also needed to determine the mechanisms by which Stasimon deficiency leads to activation of p38 MAPK-dependent pathways and whether these events are necessary and sufficient to drive SMA motor neuron death in the context of Mdm2- and Mdm4-mediated p53 upregulation.

Recent studies have shown that Stasimon is an ER-resident, six-transmembrane-pass protein that is essential for mouse embryonic development (Van Alstyne et al., 2018b) and functions in autophagy (Moretti et al., 2018; Morita et al., 2018; Shoemaker et al., 2019). There have also been reports of autophagy dysregulation in SMA, but there is disagreement about whether this pathway is inhibited (Custer and Androphy, 2014; Periyakaruppiah et al., 2016; Rodriguez-Muela et al., 2018) or stimulated (Gonçalves et al., 2018; Piras et al., 2017) by SMN deficiency. Therefore, although autophagy inhibition has been shown to ameliorate the phenotype of SMA mice by blocking p62-mediated SMN degradation (Rodriguez-Muela et al., 2018), it remains to be established whether autophagy defects directly contribute to SMA pathology. We found no evidence for overt autophagy dysregulation in the spinal motor circuit of SMA mice, suggesting that the Stasimon-dependent effects in these neurons might be mediated by disruption of other cellular functions. In that regard, Stasimon is enriched at ER-mitochondrial contact sites (Van Alstyne et al., 2018b), which are implicated in a variety of biological processes beyond autophagy that are important for neuronal physiology and disease (Paillusson et al., 2016). Elucidation of the specific cellular deficits underlying

Stasimon-dependent motor circuit pathology in SMA will require greater knowledge of the full breadth of Stasimon functions. It will also need to integrate previous, seemingly unrelated, findings linking dysregulation of endocytosis (Ackermann et al., 2013; Hosseinibarkooie et al., 2016; Janzen et al., 2018; Riessland et al., 2017) and UBA1/GARS-dependent pathways (Shorrock et al., 2018) to the loss of SMA proprioceptive synapses into a coherent model.

In summary, our work identifies Stasimon as a determinant of defective synaptic connectivity and function in the SMA sensory-motor circuit as well as an upstream trigger of a signaling cascade that feeds into p53 and the motor neuron cell death pathway through p38 MAPK activation. Moreover, MW150 is in early stage clinical trials for disorders in which p38α MAPK-mediated pathways are part of pathophysiology progression, and our findings argue for future pursuit of MW150 treatment as a potential therapeutic approach for neuroprotection in SMA.

STAR★METHODS

LEAD CONTACT AND MATERIALS AVAILABILITY

Further information and requests for resources and reagents should be directed to and will be fulfilled by the Lead Contact, Livio Pellizzoni (lp2284@cumc.columbia.edu).

All unique/stable reagents generated in this study are available from the Lead Contact with a completed Materials Transfer Agreement.

EXPERIMENTAL MODEL AND SUBJECT DETAILS

Cell Lines—The NIH 3T3-$Stas_{RNAi}$ cell line was generated by transduction of male NIH 3T3 fibroblasts with pLenti.pur/$Stas_{RNAi}$, followed by antibiotic selection with 5 μg/ml Puromycin (Sigma) and cloning by limiting dilution as described before (Lotti et al., 2012; Ruggiu et al., 2012). Mouse NIH 3T3 fibroblasts were grown in DMEM with high glucose (Invitrogen) containing 10% of FBS (HyClone), 2 mM glutamine (GIBCO), and 10 μg/mL Gentamicin (GIBCO) at 37°C.

Mouse Models—All mouse studies were performed in accordance with the NIH guidelines and approved by the Institutional Laboratory Animal Care and Use Committee (IACUC) of Columbia University (protocol # AC-AAAQ4402). Mice of both sexes in equal proportions were used in all experiments. The original breeding pairs for SMNΔ7 (*Smn*$^{+/-}$; *SMN2*$^{+/+}$; *SMNΔ7*$^{+/+}$) mice (stock #005025), PV^{Cre} mice (stock #008069), $ChAT^{Cre}$ mice (stock #006410), and Smn^{Res} (*Smn*$^{Res/+}$; *SMN2*$^{+/+}$; *SMNΔ7*$^{+/+}$) mice expressing a Cre-inducible Smn^{Res} allele (stock #007951) were obtained from Jackson Laboratory. Experimental SMA mice indicated as SMA+SMN (PV^{CRE}) and SMA+SMN ($ChAT^{CRE}$) carried one *Smn*^{Res} allele and one *Smn* knockout allele, and were heterozygous for either PV^{Cre} or $ChAT^{Cre}$ in the SMNΔ7 background (i.e., *PV*$^{Cre+/-}$; *Smn*$^{Res/-}$; *SMN2*$^{+/+}$; *SMNΔ7*$^{+/+}$ and *ChAT*$^{Cre+/-}$; *Smn*$^{Res/-}$; *SMN2*$^{+/+}$; *SMNΔ7*$^{+/+}$ respectively). These Cre-harboring SMA mice were on a mixed (C57BL6 and FVB) background, while all other experiments were performed using SMNΔ7 mice on a pure FVB background. Tail DNA

PCR genotyping was performed as described previously (Fletcher et al., 2017). See Table S1 for the sequence of all primers.

METHOD DETAILS

DNA cloning and viral production—For AAV9 production, DNA fragments corresponding to the open reading frames of GFP, human SMN (NM_000344), and human STAS (NM_015012) were generated by PCR using plasmid templates obtained from OriGene and cloned downstream of the CMV enhancer and chicken beta-actin (CB) hybrid promoter in the dsAAV-CB plasmid (a gift from Brian Kaspar) harboring AAV2 ITRs for the production of self-complementary AAV9 (Foust et al., 2010). The corresponding AAV9 vectors packaged into serotype-9 capsid were custom produced by Vector BioLabs using triple plasmid transfection of HEK293 cells and purification by two rounds of CsCl gradient centrifugation. At least two independent batches of AAV9 vectors were used in this study. Titer and purity of each AAV9 preparation were confirmed in-house by qPCR (see Table S1 for the sequence of primers) and silver staining, respectively.

For lentiviral production, complementary oligonucleotide templates for an shRNA targeting mouse Stasimon mRNA (5′-GGAAGACCCGTTGTATACA-3′) were annealed and cloned into pSUPERIOR.puro (OligoEngine). To generate the pLenti.pur/$Stas_{RNAi}$ lentiviral vector, a fragment comprising the shRNA cassette under the control of a tetracyline-regulated $H1_{TO}$ promoter and the puromycin resistance gene driven by the PGK promoter were excised from pSUPERIOR.puro and cloned into a modified pRRLSIN.cPPT.PGK-GFP.WPRE vector (Addgene plasmid 12252) lacking the PGK-GFP cassette as a backbone. Viral stocks pseudotyped with the vesicular stomatitis G protein (VSV-G) were prepared by transient co-transfection of HEK293T cells using the ViraPower Lentiviral Packaging Mix (Invitrogen) following manufacturer's instructions.

Cell treatments—NIH 3T3 cells were cultured for 4 hours in the presence of 100 nM Bafilomycin A (Alfa Aesar) to block autophagy and/or in DMEM media without glutamine and serum for autophagy induction prior to downstream analysis. For treatment with MOs, each MO (GeneTools) was added to culture media at a final concentration of 10 μM along with Endoporter (GeneTools) and incubated for 60 hours. MW150 treatment was carried out by culturing NIH 3T3 cells in the presence of 8 μM MW150 for 8 hours prior to addition of MOs. For immunofluorescence analysis following MO treatment, NIH 3T3 cells cultured on glass coverslips in 24-well plates were washed briefly with phosphate buffered saline (PBS), fixed with 4% paraformaldehyde (PFA) in PBS for 15 minutes at room temperature, and permeabilized with 0.5% Triton X-100–PBS for 10 minutes at room temperature. Blocking and incubation with both primary and secondary antibodies were performed using 3% bovine serum albumin (BSA) in PBS for 1 hour at room temperature. Images were collected with an SP5 Leica confocal microscope.

Animal procedures and behavioral analysis—All surgical procedures on postnatal mice were performed in accordance with the NIH guidelines and approved by the IACUC of Columbia University. For AAV9 gene delivery, P0 mice were anesthetized by isoflurane inhalation and injected in the right lateral ventricle of the brain with ~1x 10^{11} genome copies

of AAV9 vectors in a PBS solution containing a vital dye (Fast Green; Sigma-Aldrich). Treatment of SMA mice with MW150 (5 mg/kg) or vehicle (saline) was carried out by daily i.p. injection beginning at P0. There was no blinding of the treatment groups. Approximately equal proportions of mice of both sexes were used in all experiments, and aggregated data are presented because gender-specific differences were not found.

For behavioral analysis, mice from all experimental groups were monitored daily, weighed, and three righting reflex tests were timed and averaged as described previously (Mentis et al., 2011). Mice with 25% weight loss and an inability to right were euthanized with carbon dioxide to comply with IACUC guidelines. Righting time was defined as the time for the pup to turn over on its limbs after being placed on its back. The cut-off test time for the righting reflex was 60 s to comply with IACUC guidelines.

Immunohistochemistry—For immunostaining of the spinal cord, mice were sacrificed at P11, the spinal cord was removed natively and post-fixed in 4% PFA overnight at 4°C. On the following day, the spinal cords were briefly washed with PBS, subsequently embedded in warm 5% Agar and serial transverse sections (75 μm) were cut on a Leica VT1000S vibratome. The sections were blocked with 10% normal donkey serum in 0.01 M PBS with 0.4% Triton X-100 (PBS-T; pH 7.4) for 1.5 hours and incubated overnight at room temperature in different combinations of the primary antibodies. The following day, after six 10-minute washes with PBS, secondary antibody incubations were performed for 3 hours with the appropriate species-specific antiserum coupled to FITC, Cy3 or Cy5 (Jackson labs) diluted at 1:250 in PBS-T. After secondary antibody incubations, the sections were washed six times for 10 minutes in PBS and mounted on slides and coverslipped with an anti-fading solution made of Glycerol:PBS (3:7).

For immunostaining of NMJs, mice were sacrificed at P11 and the QL muscle was dissected and immediately fixed with 4% PFA for 20 minutes. After fixation, single muscle fibers were teased and washed five times in PBS for 10 minutes each followed by staining of the postsynaptic part of the NMJ with α-bungarotoxin coupled to Alexa Fluor 555 in PBS for 20 minutes. Subsequently, the muscle fibers were washed five times in PBS for 10 minutes and blocked with 10% donkey serum in PBS-T for 1 hour. Anti-Neurofilament-M and anti-Synaptophysin 1 antibodies to immunolabel the presynaptic part of the NMJ were applied in blocking solution overnight at 4°C. The muscle fibers were then washed 3 times for 10 minutes in PBS. Secondary antibodies were applied for 1 hour in blocking solution at room temperature. Finally, the muscle fibers were washed 3 times in PBS for 10 minutes and mounted with Vectashield (Vector laboratories, CA) (Simon et al., 2017).

Confocal microscopy—Confocal microscopy was performed using either SP5 or SP8 (Leica) confocal microscopes as described previously (Simon et al., 2017; Van Alstyne et al., 2018a). Sections were scanned using a 20x or 40x objective. Motor neurons were counted offline from z stack images (collected at 3 μm intervals in the z axis) from eleven sections of the selected L1 and L5 spinal segments as we previously described (Simon et al., 2017; Van Alstyne et al., 2018a). Only ChAT+ motor neurons that contained the nucleus were counted to avoid double counting from adjoining sections. Quantitative analysis of VGluT1 immunoreactive synaptic densities on motor neurons was performed on image

stacks of optical sections scanned using a 40x oil (N.A. 1.25) objective throughout the whole section thickness at 0.3 μm z-steps to include the whole cell body and dendrites of $ChAT^+$ motor neurons. The number of $VGluT1^+$ synapses were counted over the entire surface of the motor neuron soma as well as on primary dendrites up to a distance of 100 μm from the soma using Leica LASAF software as previously described (Mentis et al., 2011). For the analysis of muscle innervation, at least 200 randomly selected NMJs per muscle sample were quantified for each biological replicate. Only BTX^+ endplates that lacked any pre-synaptic coverage by both synaptophysin and NF-M were scored as fully denervated.

Electrophysiology—To record the monosynaptic reflex, we conducted the experiment as previously described (Simon et al., 2017). The animals were decapitated at P11, the spinal cords dissected and removed under cold (~12°C) artificial cerebrospinal fluid (aCSF) containing 128.35 mM NaCl, 4 mM KCl, 0.58 mM $NaH_2PO_4.H_20$, 21 mM $NaHCO_3$, 30 mM D-Glucose, 1.5 mM $CaCl_2.H_20$, and 1 mM $MgSO_4.7H_20$. The spinal cord was then transferred to a customized recording chamber. The intact *ex vivo* spinal cord preparation was perfused continuously with oxygenated ($95\%O_2/5\%CO_2$) aCSF (~13 ml/min). The dorsal root and ventral root of the L1 segment were placed into suction electrodes for stimulation or recording, respectively. The extracellular ventral root potentials were recorded (DC – 3 kHz, Cyberamp, Molecular Devices) in response to a brief (0.2 ms) orthodromic stimulation (A365, current stimulus isolator, WPI, Sarasota, FL) of the L1 dorsal root. The stimulus threshold was defined as the current at which the minimal evoked response was recorded in three out of five trials. Recordings were fed to an A/D interface (Digidata 1440A, Molecular Devices) and acquired with Clampex (v10.2, Molecular Devices) at a sampling rate of 10 kHz. Data were analyzed offline using Clampfit (v10.2, Molecular Devices). The monosynaptic component of the EPSP amplitude was measured from the onset of response to 3 ms . Measurements were taken from averaged traces of five trials elicited at 0.1 Hz. The temperature of the physiological solution ranged between 21-25°C. For synaptic depression experiments, the dorsal root was stimulated at 10 Hz for five stimuli and the resulting monosynaptic component of the amplitude recorded and analyzed offline. The amplitude of the second to the fifth stimulus was expressed as a percentage of the amplitude of the first stimulus.

To functionally assess NMJs of the QL muscle at P11, we applied the same technique as described previously (Fletcher et al., 2017). Motor neurons axons in the ventral root L1 supplying the QL muscle were stimulated by drawing the ventral root into a suction electrode, having removed the spinal cord, and the CMAP was recorded from the muscle using a concentric bipolar electrode. L1 motor neuron axons were stimulated with five stimuli at 0.1 Hz. The maximum CMAP amplitude (baseline-to-peak) was measured from five averages.

RNA and protein analysis—For RNA analysis from NIH 3T3 cells and mouse tissue, total RNA purification and qRT-PCR experiments were carried out as previously described (Lotti et al., 2012; Van Alstyne et al., 2018a). The primers used are listed in Table S1. For protein analysis, NIH 3T3 cells and mouse tissues were homogenized directly in SDS-PAGE

sample buffer and electrophoresed on a 12% SDS-PAGE gel followed by western blotting as previously described (Ruggiu et al., 2012).

QUANTIFICATION AND STATISTICAL ANALYSIS

Results are expressed as mean ± standard error of the mean (SEM) from at least three independent experiments using three or more animals per group. The exact value and meaning of n for each dataset can be found in the figure legends. Differences between two groups were analyzed by a two-tailed unpaired Student's t test, whereas differences among three or more groups were analyzed by one-way or two-way ANOVA followed by Tukey's correction for multiple comparisons as applicable. GraphPad Prism 6 was used for all statistical analyses and P values are indicated as follows: * = $p < 0.05$; ** = $p < 0.01$; *** = $p < 0.001$.

DATA AND CODE AVAILABILITY

This study did not generate any unique datasets or code.

Supplementary Material

Refer to Web version on PubMed Central for supplementary material.

ACKNOWLEDGMENTS

We are grateful to Dr. Brian Kaspar for the kind gift of the dsAAV-CB plasmid. This work was supported by the SMA Foundation (L.P. and G.Z.M.), a grant from Cure SMA (L.P.), and NIH grants R01NS078375 and R01AA027079 (G.Z.M.) and R21NS077038, R21NS098363, and R01NS102451 (L.P.).

REFERENCES

Ackermann B, Kröber S, Torres-Benito L, Borgmann A, Peters M, Hosseini Barkooie SM, Tejero R, Jakubik M, Schreml J, Milbradt J, et al. (2013). Plastin 3 ameliorates spinal muscular atrophy via delayed axon pruning and improves neuromuscular junction functionality. Hum. Mol. Genet 22, 1328–1347. [PubMed: 23263861]

Bäumer D, Lee S, Nicholson G, Davies JL, Parkinson NJ, Murray LM, Gillingwater TH, Ansorge O, Davies KE, and Talbot K (2009). Alternative splicing events are a late feature of pathology in a mouse model of spinal muscular atrophy. PLoS Genet. 5, e1000773. [PubMed: 20019802]

Bebee TW, Dominguez CE, Samadzadeh-Tarighat S, Akehurst KL, and Chandler DS (2012). Hypoxia is a modifier of SMN2 splicing and disease severity in a severe SMA mouse model. Hum. Mol. Genet 21, 4301–4313. [PubMed: 22763238]

Boulisfane N, Choleza M, Rage F, Neel H, Soret J, and Bordonné R (2011). Impaired minor tri-snRNP assembly generates differential splicing defects of U12-type introns in lymphoblasts derived from a type I SMA patient. Hum. Mol. Genet 20, 641–648. [PubMed: 21098506]

Burghes AHM, and Beattie CE (2009). Spinal muscular atrophy: why do low levels of survival motor neuron protein make motor neurons sick? Nat. Rev. Neurosci 10, 597–609. [PubMed: 19584893]

Custer SK, and Androphy EJ (2014). Autophagy dysregulation in cell culture and animals models of spinal muscular atrophy. Mol. Cell. Neurosci 61, 133–140. [PubMed: 24983518]

Doktor TK, Hua Y, Andersen HS, Brøner S, Liu YH, Wieckowska A, Dembic M, Bruun GH, Krainer AR, and Andresen BS (2017). RNA-sequencing of a mouse-model of spinal muscular atrophy reveals tissue-wide changes in splicing of U12-dependent introns. Nucleic Acids Res. 45, 395–16. [PubMed: 27557711]

Donlin-Asp PG, Bassell GJ, and Rossoll W (2016). A role for the survival of motor neuron protein in mRNP assembly and transport. Curr. Opin. Neurobiol 39, 53–61. [PubMed: 27131421]

Donlin-Asp PG, Fallini C, Campos J, Chou C-C, Merritt ME, Phan HC, Bassell GJ, and Rossoll W (2017). The survival of motor neuron protein acts as a molecular chaperone for mRNP assembly. Cell Rep. 18, 1660–1673. [PubMed: 28199839]

Fletcher EV, Simon CM, Pagiazitis JG, Chalif JI, Vukojicic A, Drobac E, Wang X, and Mentis GZ (2017). Reduced sensory synaptic excitation impairs motor neuron function via Kv2.1 in spinal muscular atrophy. Nat. Neurosci 20, 905–916. [PubMed: 28504671]

Foust KD, Wang X, McGovern VL, Braun L, Bevan AK, Haidet AM, Le TT, Morales PR, Rich MM, Burghes AHM, and Kaspar BK (2010). Rescue of the spinal muscular atrophy phenotype in a mouse model by early postnatal delivery of SMN. Nat. Biotechnol 28, 271–274. [PubMed: 20190738]

Gavrilina TO, McGovern VL, Workman E, Crawford TO, Gogliotti RG, DiDonato CJ, Monani UR, Morris GE, and Burghes AHM (2008). Neuronal SMN expression corrects spinal muscular atrophy in severe SMA mice while muscle-specific SMN expression has no phenotypic effect. Hum. Mol. Genet 17, 1063–1075. [PubMed: 18178576]

Genabai NK, Ahmad S, Zhang Z, Jiang X, Gabaldon CA, and Gangwani L (2015). Genetic inhibition of JNK3 ameliorates spinal muscular atrophy. Hum. Mol. Genet 24, 6986–7004. [PubMed: 26423457]

Gogliotti RG, Quinlan KA, Barlow CB, Heier CR, Heckman CJ, and Didonato CJ (2012). Motor neuron rescue in spinal muscular atrophy mice demonstrates that sensory-motor defects are a consequence, not a cause, of motor neuron dysfunction. J. Neurosci 32, 3818–3829. [PubMed: 22423102]

Gonçalves IDCG, Brecht J, Thelen MP, Rehorst WA, Peters M, Lee HJ, Motameny S, Torres-Benito L, Ebrahimi-Fakhari D, Kononenko NL, et al. (2018). Neuronal activity regulates DROSHA via autophagy in spinal muscular atrophy. Sci. Rep 8, 7907. [PubMed: 29784949]

Groen EJN, Talbot K, and Gillingwater TH (2018). Advances in therapy for spinal muscular atrophy: promises and challenges. Nat. Rev. Neurol 14, 214–224. [PubMed: 29422644]

Hosseinibarkooie S, Peters M, Torres-Benito L, Rastetter RH, Hupperich K, Hoffmann A, Mendoza-Ferreira N, Kaczmarek A, Janzen E, Milbradt J, et al. (2016). The power of human protective modifiers: PLS3 and CORO1C unravel impaired endocytosis in spinal muscular atrophy and rescue SMA phenotype. Am. J. Hum. Genet 99, 647–665. [PubMed: 27499521]

Hua Y, Liu YH, Sahashi K, Rigo F, Bennett CF, and Krainer AR (2015). Motor neuron cell-nonautonomous rescue of spinal muscular atrophy phenotypes in mild and severe transgenic mouse models. Genes Dev. 29, 288–297. [PubMed: 25583329]

Imlach WL, Beck ES, Choi BJ, Lotti F, Pellizzoni L, and McCabe BD (2012). SMN is required for sensory-motor circuit function in *Drosophila*. Cell 151, 427–439. [PubMed: 23063130]

Iyer CC, McGovern VL, Murray JD, Gombash SE, Zaworski PG, Foust KD, Janssen PML, and Burghes AHM (2015). Low levels of survival motor neuron protein are sufficient for normal muscle function in the SMNΔ7 mouse model of SMA. Hum. Mol. Genet 24, 6160–6173. [PubMed: 26276812]

Jangi M, Fleet C, Cullen P, Gupta SV, Mekhoubad S, Chiao E, Allaire N, Bennett CF, Rigo F, Krainer AR, et al. (2017). SMN deficiency in severe models of spinal muscular atrophy causes widespread intron retention and DNA damage. Proc. Natl. Acad. Sci. USA 114, E2347–E2356. [PubMed: 28270613]

Janzen E, Mendoza-Ferreira N, Hosseinibarkooie S, Schneider S, Hupperich K, Tschanz T, Grysko V, Riessland M, Hammerschmidt M, Rigo F, et al. (2018). CHP1 reduction ameliorates spinal muscular atrophy pathology by restoring calcineurin activity and endocytosis. Brain 141, 2343–2361. [PubMed: 29961886]

Jodelka FM, Ebert AD, Duelli DM, and Hastings ML (2010). A feedback loop regulates splicing of the spinal muscular atrophy-modifying gene, SMN2. Hum. Mol. Genet 19, 4906–4917. [PubMed: 20884664]

Kannan A, Bhatia K, Branzei D, and Gangwani L (2018). Combined deficiency of Senataxin and DNA-PKcs causes DNA damage accumulation and neurodegeneration in spinal muscular atrophy. Nucleic Acids Res. 46, 8326–8346. [PubMed: 30010942]

Kim J-K, Caine C, Awano T, Herbst R, and Monani UR (2017). Motor neuronal repletion of the NMJ organizer, Agrin, modulates the severity of the spinal muscular atrophy disease phenotype in model mice. Hum. Mol. Genet 26, 2377–2385. [PubMed: 28379354]

Le TT, Pham LT, Butchbach MER, Zhang HL, Monani UR, Coovert DD, Gavrilina TO, Xing L, Bassell GJ, and Burghes AHM (2005). SMNΔ7, the major product of the centromeric survival motor neuron (SMN2) gene, extends survival in mice with spinal muscular atrophy and associates with full-length SMN. Hum. Mol. Genet 14, 845–857. [PubMed: 15703193]

Lefebvre S, Bürglen L, Reboullet S, Clermont O, Burlet P, Viollet L, Benichou B, Cruaud C, Millasseau P, Zeviani M, et al. (1995). Identification and characterization of a spinal muscular atrophy-determining gene. Cell 80, 155–165. [PubMed: 7813012]

Li DK, Tisdale S, Lotti F, and Pellizzoni L (2014). SMN control of RNP assembly: from post-transcriptional gene regulation to motor neuron disease. Semin. Cell Dev. Biol 32, 22–29. [PubMed: 24769255]

Lotti F, Imlach WL, Saieva L, Beck ES, Hao T, Li DK, Jiao W, Mentis GZ, Beattie CE, McCabe BD, and Pellizzoni L (2012). An SMN-dependent U12 splicing event essential for motor circuit function. Cell 151, 440–454. [PubMed: 23063131]

Lutz CM, Kariya S, Patruni S, Osborne MA, Liu D, Henderson CE, Li DK, Pellizzoni L, Rojas J, Valenzuela DM, et al. (2011). Postsymptomatic restoration of SMN rescues the disease phenotype in a mouse model of severe spinal muscular atrophy. J. Clin. Invest 121, 3029–3041. [PubMed: 21785219]

Martinez TL, Kong L, Wang X, Osborne MA, Crowder ME, Van Meerbeke JP, Xu X, Davis C, Wooley J, Goldhamer DJ, et al. (2012). Survival motor neuron protein in motor neurons determines synaptic integrity in spinal muscular atrophy. J. Neurosci 32, 8703–8715. [PubMed: 22723710]

McGovern VL, Iyer CC, Arnold WD, Gombash SE, Zaworski PG, Blatnik AJ 3rd, Foust KD, and Burghes AHM (2015). SMN expression is required in motor neurons to rescue electrophysiological deficits in the SMNΔ7 mouse model of SMA. Hum. Mol. Genet 24, 5524–5541. [PubMed: 26206889]

Meister G, Bühler D, Pillai R, Lottspeich F, and Fischer U (2001). A multi-protein complex mediates the ATP-dependent assembly of spliceosomal U snRNPs. Nat. Cell Biol 3, 945–949. [PubMed: 11715014]

Mendelsohn AI, Simon CM, Abbott LF, Mentis GZ, and Jessell TM (2015). Activity regulates the incidence of heteronymous sensory-motor connections. Neuron 87, 111–123. [PubMed: 26094608]

Mentis GZ, Blivis D, Liu W, Drobac E, Crowder ME, Kong L, Alvarez FJ, Sumner CJ, and O'Donovan MJ (2011). Early functional impairment of sensory-motor connectivity in a mouse model of spinal muscular atrophy. Neuron 69, 453–467. [PubMed: 21315257]

Miller N, Feng Z, Edens BM, Yang B, Shi H, Sze CC, Hong BT, Su SC, Cantu JA, Topczewski J, et al. (2015). Non-aggregating tau phosphorylation by cyclin-dependent kinase 5 contributes to motor neuron degeneration in spinal muscular atrophy. J. Neurosci 35, 6038–6050. [PubMed: 25878277]

Moretti F, Bergman P, Dodgson S, Marcellin D, Claerr I, Goodwin JM, DeJesus R, Kang Z, Antczak C, Begue D, et al. (2018). TMEM41B is a novel regulator of autophagy and lipid mobilization. EMBO Rep. 19, e45889. [PubMed: 30126924]

Morita K, Hama Y, Izume T, Tamura N, Ueno T, Yamashita Y, Sakamaki Y, Mimura K, Morishita H, Shihoya W, et al. (2018). Genome-wide CRISPR screen identifies TMEM41B as a gene required for autophagosome formation. J. Cell Biol 217, 3817–3828. [PubMed: 30093494]

Ng S-Y, Soh BS, Rodriguez-Muela N, Hendrickson DG, Price F, Rinn JL, and Rubin LL (2015). Genome-wide RNA-seq of human motor neurons implicates selective ER stress activation in spinal muscular atrophy. Cell Stem Cell 17, 569–584. [PubMed: 26321202]

Paillusson S, Stoica R, Gomez-Suaga P, Lau DHW, Mueller S, Miller T, and Miller CCJ (2016). There's something wrong with my MAM; the ER-mitochondria axis and neurodegenerative diseases. Trends Neurosci. 39, 146–157. [PubMed: 26899735]

Passini MA, Bu J, Roskelley EM, Richards AM, Sardi SP, O'Riordan CR, Klinger KW, Shihabuddin LS, and Cheng SH (2010). CNS-targeted gene therapy improves survival and motor function in a mouse model of spinal muscular atrophy. J. Clin. Invest 120, 1253–1264. [PubMed: 20234094]

Pellizzoni L, Yong J, and Dreyfuss G (2002). Essential role for the SMN complex in the specificity of snRNP assembly. Science 298, 1775–1779. [PubMed: 12459587]

Periyakaruppiah A, de la Fuente S, Arumugam S, Bahí N, Garcera A, and Soler RM(2016).Autophagy modulators regulate survival motor neuron protein stability in motoneurons. Exp. Neurol 283 (Pt A), 287–297. [PubMed: 27373203]

Pilato CM, Park JH, Kong L, d'Ydewalle C, Valdivia D, Chen KS, Griswold-Prenner I, and Sumner CJ (2019). Motor neuron loss in SMA is not associated with somal stress-activated JNK/c-Jun signaling. Hum. Mol. Genet 28, 3282–3292. [PubMed: 31272106]

Pillai RS, Grimmler M, Meister G, Will CL, Lührmann R, Fischer U, and Schümperli D (2003). Unique Sm core structure of U7 snRNPs: assembly by a specialized SMN complex and the role of a new component, Lsm11, in histone RNA processing. Genes Dev. 17, 2321–2333. [PubMed: 12975319]

Piras A, Schiaffino L, Boido M, Valsecchi V, Guglielmotto M, De Amicis E, Puyal J, Garcera A, Tamagno E, Soler RM, and Vercelli A (2017). Inhibition of autophagy delays motoneuron degeneration and extends lifespan in a mouse model of spinal muscular atrophy. Cell Death Dis. 8, 3223. [PubMed: 29259166]

Plotnikov A, Zehorai E, Procaccia S, and Seger R (2011). The MAPK cascades: signaling components, nuclear roles and mechanisms of nuclear translocation. Biochim. Biophys. Acta 1813, 1619–1633. [PubMed: 21167873]

Riessland M, Kaczmarek A, Schneider S, Swoboda KJ, Löhr H, Bradler C, Grysko V, Dimitriadi M, Hosseinibarkooie S, Torres-Benito L, et al. (2017). Neurocalcin delta suppression protects against spinal muscular atrophy in humans and across species by restoring impaired endocytosis. Am. J. Hum. Genet 100, 297–315. [PubMed: 28132687]

Robbins KL, Glascock JJ, Osman EY, Miller MR, and Lorson CL (2014). Defining the therapeutic window in a severe animal model of spinal muscular atrophy. Hum. Mol. Genet 23, 4559–4568. [PubMed: 24722206]

Robson MJ, Quinlan MA, Margolis KG, Gajewski-Kurdziel PA, Veenstra-VanderWeele J, Gershon MD, Watterson DM, and Blakely RD (2018). p38α MAPK signaling drives pharmacologically reversible brain and gastrointestinal phenotypes in the SERT Ala56 mouse. Proc. Natl. Acad. Sci. USA 115, E10245–E10254. [PubMed: 30297392]

Rodriguez-Muela N, Parkhitko A, Grass T, Gibbs RM, Norabuena EM, Perrimon N, Singh R, and Rubin LL (2018). Blocking p62-dependent SMN degradation ameliorates spinal muscular atrophy disease phenotypes. J. Clin. Invest 128, 3008–3023. [PubMed: 29672276]

Roy SM, Grum-Tokars VL, Schavocky JP, Saeed F, Staniszewski A, Teich AF, Arancio O, Bachstetter AD, Webster SJ, Van Eldik LJ, et al. (2015). Targeting human central nervous system protein kinases: An isoform selective p38αMAPK inhibitor that attenuates disease progression in Alzheimer's disease mouse models. ACS Chem. Neurosci 6, 666–680. [PubMed: 25676389]

Roy SM, Minasov G, Arancio O, Chico LW, Van Eldik LJ, Anderson WF, Pelletier JC, and Watterson DM (2019). A selective and brain penetrant p38αMAPK inhibitor candidate for neurologic and neuropsychiatric disorders that attenuates neuroinflammation and cognitive dysfunction. J. Med. Chem 62, 5298–5311. [PubMed: 30978288]

Ruggiu M, McGovern VL, Lotti F, Saieva L, Li DK, Kariya S, Monani UR, Burghes AHM, and Pellizzoni L (2012). A role for SMN exon 7 splicing in the selective vulnerability of motor neurons in spinal muscular atrophy. Mol. Cell. Biol 32, 126–138. [PubMed: 22037760]

Rutigliano G, Stazi M, Arancio O, Watterson DM, and Origlia N (2018). An isoform-selective p38α mitogen-activated protein kinase inhibitor rescues early entorhinal cortex dysfunctions in a mouse model of Alzheimer's disease. Neurobiol. Aging 70, 86–91. [PubMed: 30007168]

Sahashi K, Hua Y, Ling KKY, Hung G, Rigo F, Horev G, Katsuno M, Sobue G, Ko C-P, Bennett CF, and Krainer AR (2012). TSUNAMI: an antisense method to phenocopy splicing-associated diseases in animals. Genes Dev. 26, 1874–1884. [PubMed: 22895255]

Shoemaker CJ, Huang TQ, Weir NR, Polyakov NJ, Schultz SW, and Denic V (2019). CRISPR screening using an expanded toolkit of autophagy reporters identifies TMEM41B as a novel autophagy factor. PLoS Biol. 17, e2007044. [PubMed: 30933966]

Shorrock HK, van der Hoorn D, Boyd PJ, Llavero Hurtado M, Lamont DJ, Wirth B, Sleigh JN, Schiavo G, Wishart TM, Groen EJN, and Gillingwater TH (2018). UBA1/GARS-dependent pathways drive sensory-motor connectivity defects in spinal muscular atrophy. Brain 141, 2878–2894. [PubMed: 30239612]

Shorrock HK, Gillingwater TH, and Groen EJN (2019). Molecular mechanisms underlying sensory-motor circuit dysfunction in SMA. Front. Mol. Neurosci 12, 59. [PubMed: 30886572]

Simon CM, Janas AM, Lotti F, Tapia JC, Pellizzoni L, and Mentis GZ (2016). A stem cell model of the motor circuit uncouples motor neuron death from hyperexcitability induced by SMN deficiency. Cell Rep. 16, 1416–1430. [PubMed: 27452470]

Simon CM, Dai Y, Van Alstyne M, Koutsioumpa C, Pagiazitis JG, Chalif JI, Wang X, Rabinowitz JE, Henderson CE, Pellizzoni L, and Mentis GZ (2017). Converging mechanisms of p53 activation drive motor neuron degeneration in spinal muscular atrophy. Cell Rep. 21, 3767–3780. [PubMed: 29281826]

Tisdale S, and Pellizzoni L (2015). Disease mechanisms and therapeutic approaches in spinal muscular atrophy. J. Neurosci 35, 8691–8700. [PubMed: 26063904]

Tisdale S, Lotti F, Saieva L, Van Meerbeke JP, Crawford TO, Sumner CJ, Mentis GZ, and Pellizzoni L (2013). SMN is essential for the biogenesis of U7 small nuclear ribonucleoprotein and 3′-end formation of histone mRNAs. Cell Rep. 5, 1187–1195. [PubMed: 24332368]

Toledo F, and Wahl GM (2006). Regulating the p53 pathway: in vitro hypotheses, in vivo veritas. Nat. Rev. Cancer 6, 909–923. [PubMed: 17128209]

Van Alstyne M, and Pellizzoni L (2016). Advances in modeling and treating spinal muscular atrophy. Curr. Opin. Neurol 29, 549–556. [PubMed: 27472505]

Van Alstyne M, Simon CM, Sardi SP, Shihabuddin LS, Mentis GZ, and Pellizzoni L (2018a). Dysregulation of Mdm2 and Mdm4 alternative splicing underlies motor neuron death in spinal muscular atrophy. Genes Dev. 32, 1045–1059. [PubMed: 30012555]

Van Alstyne M, Lotti F, Dal Mas A, Area-Gomez E, and Pellizzoni L (2018b). Stasimon/Tmem41b localizes to mitochondria-associated ER membranes and is essential for mouse embryonic development. Biochem. Biophys. Res. Commun 506, 463–470. [PubMed: 30352685]

Vousden KH, and Prives C (2009). Blinded by the light: the growing complexity of p53. Cell 137, 413–431. [PubMed: 19410540]

Watterson DM, Grum-Tokars VL, Roy SM, Schavocky JP, Bradaric BD, Bachstetter AD, Xing B, Dimayuga E, Saeed F, Zhang H, et al. (2013). Development of novel in vivo chemical probes to address CNS protein kinase involvement in synaptic dysfunction. PLoS ONE 8, e66226. [PubMed: 23840427]

Wu C-Y, Whye D, Glazewski L, Choe L, Kerr D, Lee KH, Mason RW, and Wang W (2011). Proteomic assessment of a cell model of spinal muscular atrophy. BMC Neurosci. 12, 25. [PubMed: 21385431]

Zhang Z, Lotti F, Dittmar K, Younis I, Wan L, Kasim M, and Dreyfuss G (2008). SMN deficiency causes tissue-specific perturbations in the repertoire of snRNAs and widespread defects in splicing. Cell 133, 585–600. [PubMed: 18485868]

Zhang Z, Pinto AM, Wan L, Wang W, Berg MG, Oliva I, Singh LN, Dengler C, Wei Z, and Dreyfuss G (2013). Dysregulation of synaptogenesis genes antecedes motor neuron pathology in spinal muscular atrophy. Proc. Natl. Acad. Sci. USA 110, 19348–19353. [PubMed: 24191055]

Zhou Z, Bachstetter AD, Späni CB, Roy SM, Watterson DM, and Van Eldik LJ (2017). Retention of normal glia function by an isoform-selective protein kinase inhibitor drug candidate that modulates cytokine production and cognitive outcomes. J. Neuroinflammation 14, 75. [PubMed: 28381303]

Highlights

- AAV9-mediated Stasimon expression improves motor function in SMA mice
- Stasimon contributes to deafferentation and motor neuron death in SMA mice
- Stasimon deficiency induces p53 phosphorylation through p38 MAPK activation
- Pharmacological inhibition of p38 MAPK prevents neurodegeneration in SMA mice

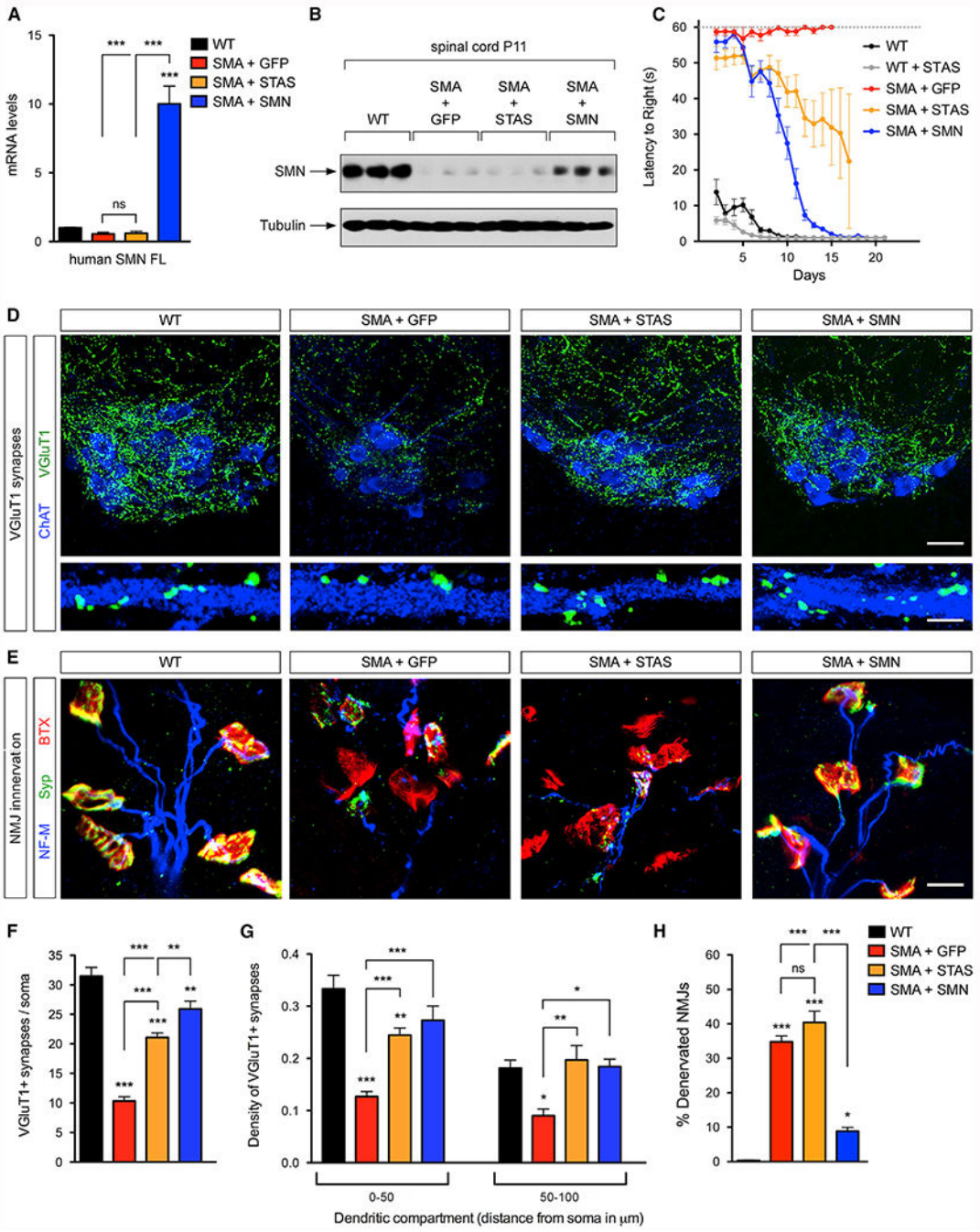

Figure 1. AAV9-Mediated Stasimon Gene Delivery in SMA Mice Improves Motor Function and Rescues the Loss of Proprioceptive Synapses on Motor Neurons

(A) qRT-PCR analysis of full-length human SMN (SMN FL) mRNA in the spinal cord of SMA mice injected with AAV9-GFP, AAV9-STAS, or AAV9-SMN as well as uninjected WT mice at P11. Data represent means and SEM (n = 6). Statistics were performed with one-way ANOVA with Tukey's post hoc test. ***p < 0.001; ns, not significant.

(B) Western blot analysis of SMN protein levels in the spinal cord of AAV9-injected SMA mice and uninjected WT controls at P11.

(C) Righting time of uninjected (n = 10) and AAV9-STAS-injected (n = 10) WT mice as well as SMA mice injected with AAV9-GFP (n = 10), AAV9-STAS (n = 24), and AAV9-SMN (n = 15). Data represent means and SEM.
(D) Immunostaining of VGluT1$^+$ synapses (green) and ChAT$^+$ motor neurons (blue) in L1 spinal cord sections from SMA mice injected with AAV9-GFP, AAV9-STAS, or AAV9-SMN as well as uninjected WT mice at P11. Scale bar: 50 μm. Bottom panels show a magnified view of VGluT1 synaptic density on proximal dendrites. Scale bar: 5 μm.
(E) NMJ staining with bungarotoxin (BTX, red), Synaptophysin (Syp, green), and Neurofilament M (NF-M, blue) of QL muscles from the same groups as in (D) at P11. Scale bar: 15 μm.
(F) Number of VGluT1$^+$ synapses on the somata of L1 motor neurons from the same groups as in (D) at P11. Data represent means and SEM from WT (n = 22), SMA+AAV9-GFP (n = 35), SMA+AAV9-STAS (n = 32), and SMA+AAV9-SMN (n = 21). Statistics were performed with one-way ANOVA with Tukey's post hoc test. **$p < 0.01$, ***$p < 0.001$.
(G) Density of VGluT1$^+$ synapses on the proximal dendrites of L1 motor neurons from the same groups as in (D) at P11. Two dendritic compartments were defined based on distance from the soma. Number of dendrites scored from the 0–50-μm compartment: WT (n = 27), SMA+AAV9-GFP (n = 21), SMA+AAV9-STAS (n = 20), and SMA+AAV9-SMN (n = 15). Number of dendrites scored from the 50–100-μm compartment: WT (n = 12), SMA+AAV9-GFP (n = 14), SMA+AAV9-STAS (n = 10), and SMA+AAV9-SMN (n = 8). Data represent means and SEM. Statistics were performed with one-way ANOVA with Tukey's post hoc test. *$p < 0.05$, **$p < 0.01$, ***$p < 0.001$.
(H) Percentage of fully denervated NMJs in the QL muscle from the same groups as in (E) at P11. Data represent means and SEM (n = 5). Statistics were performed with one-way ANOVA with Tukey's post hoc test. *$p < 0.05$, ***$p < 0.001$; ns, not significant.
See also Figure S1 and Table S1.

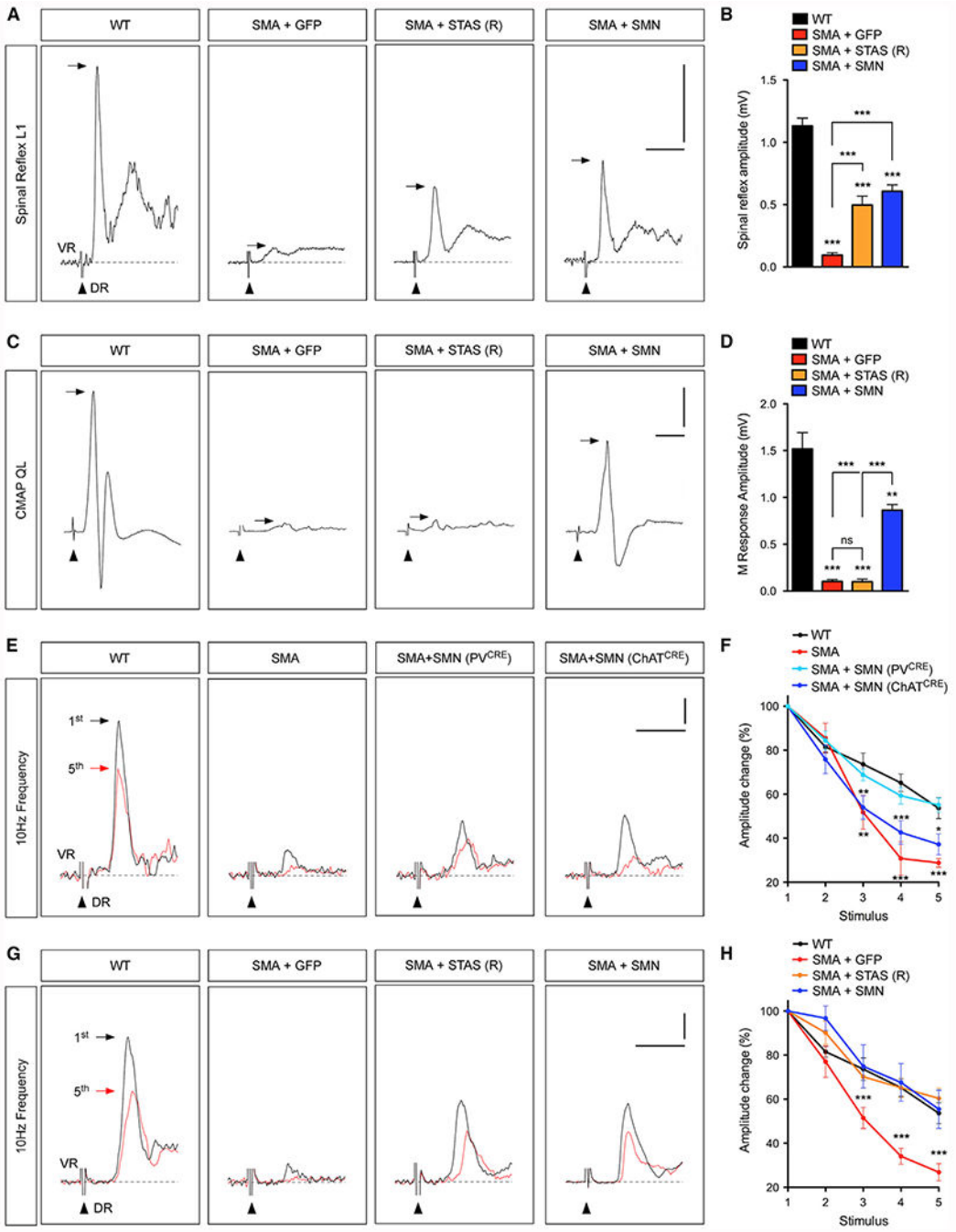

Figure 2. AAV9-STAS Acts in Proprioceptive Neurons to Improve Sensory-Motor Neurotransmission in SMA Mice

(A) Representative traces of extracellular recordings from L1 ventral root (VR) after L1 dorsal root (DR) supramaximal stimulation from SMA mice injected with AAV9-GFP, AAV9-STAS, or AAV9-SMN as well as uninjected WT mice at P11. Arrows indicate the maximum amplitude of the monosynaptic reflex. Arrowheads indicate the stimulus artifact. Scale bars: 0.5 mV and 10 ms.

(B) Quantification of spinal reflex amplitudes recorded from the same groups as in (A) at P11. Data represent means and SEM ($n \geq 4$). Statistics were performed with one-way ANOVA with Tukey's post hoc test. ***$p < 0.001$.

(C) CMAP recordings from the QL muscle after L1 ventral root stimulation in the same groups as in (A) at P11. Arrows indicate maximum amplitude. Arrowheads indicate the stimulus artifact. Scale bars: 0.5 mV and 5 ms.

(D) Quantification of M response amplitudes recorded from the QL muscle in the same groups as in (A) at P11. Data represent means and SEM ($n \geq 3$). Statistics were performed with one-way ANOVA with Tukey's post hoc test. **$p < 0.01$, ***$p < 0.001$; ns, not significant.

(E) Representative traces of the first (black) and fifth (red) ventral root (VR) responses recorded after stimulation of the homonymous L1 dorsal root (DR) at 10 Hz from WT and SMA mice as well as SMA mice with selective SMN restoration in either proprioceptive neurons (PV^{CRE}) or motor neurons ($ChAT^{CRE}$) at P11. Arrows indicate the maximum amplitude of the monosynaptic reflex. Arrowheads indicate the stimulus artifact. Scale bars: 0.2 mV and 5 ms.

(F) Quantification of amplitude changes in the monosynaptic reflex after 10-Hz stimulation from the same groups as in (E). Data represent means and SEM ($n \geq 5$). Statistics were performed with two-way ANOVA with Tukey's post hoc test, and significance relative to WT is shown. *$p < 0.05$, **$p < 0.01$, ***$p < 0.001$.

(G) Representative traces of the first (black) and fifth (red) VR responses recorded at P11 after stimulation of the homonymous L1 DR at 10 Hz from the same groups as in (A). Scale bars: 0.2 mV and 5 ms.

(H) Quantification of amplitude changes in the monosynaptic reflex after 10 Hz stimulation from the same groups as in (A). Data represent means and SEM ($n \geq 3$). Statistics were performed with two-way ANOVA with Tukey's post hoc test, and significance relative to WT is shown. ***$p < 0.001$.

See also Figure S2.

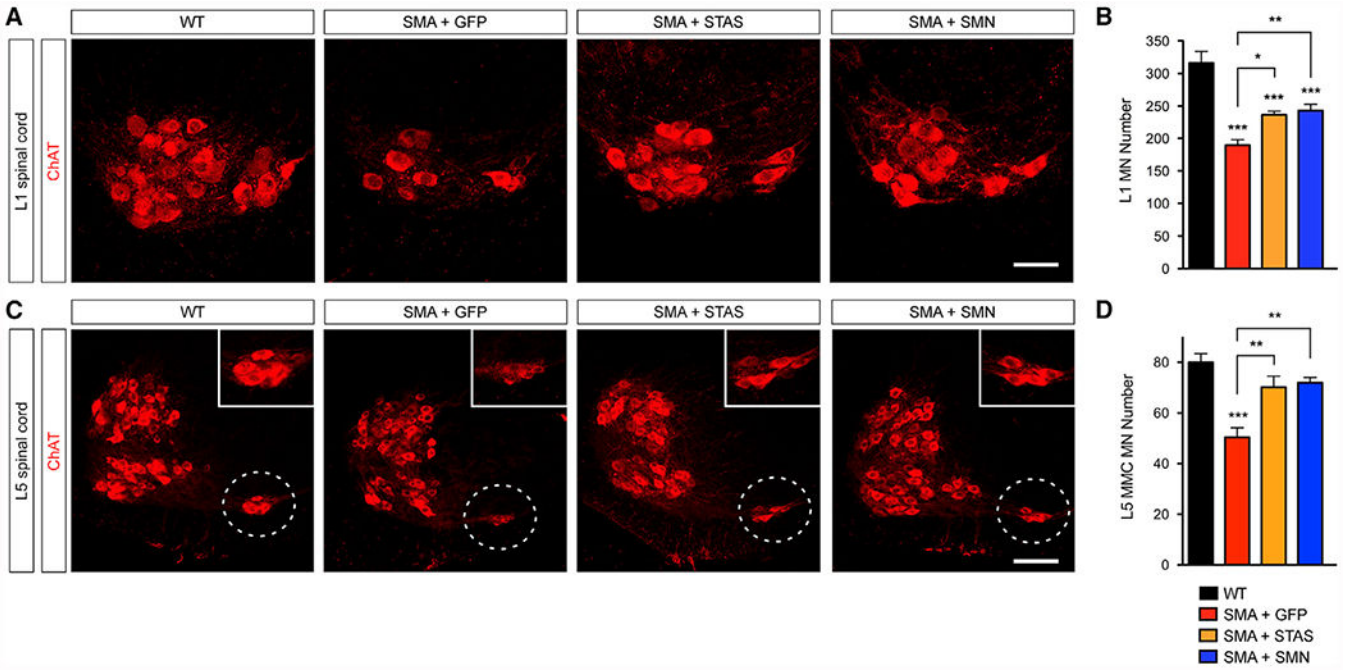

Figure 3. AAV9-STAS Rescues Vulnerable SMA Motor Neurons from Degeneration

(A) ChAT immunostaining of L1 spinal cords from SMA mice injected with AAV9-GFP, AAV9-STAS, or AAV9-SMN as well as uninjected WT mice at P11. Scale bar: 50 μm.

(B) Total number of L1 motor neurons in the same groups as in (A) at P11. Data represent means and SEM from WT (n = 4), SMA+AAV9-GFP (n = 6), SMA+AAV9-STAS (n = 7), and SMA+AAV9-SMN (n = 6). Statistics were performed with one-way ANOVA with Tukey's post hoc test. *p < 0.05, **p < 0.01, ***p < 0.001.

(C) ChAT immunostaining of L5 spinal cords from the same groups as in (A) at P11. L5 MMC motor neurons are indicated by dotted circles and magnified in the insets. Scale bar: 125 mm.

(D) Total number of L5 MMC motor neurons in the same groups as in (A) at P11. Data represent means and SEM from WT (n = 5), SMA+AAV9-GFP (n = 5), SMA+AAV9-STAS (n = 7), and SMA+AAV9-SMN (n = 6). Statistics were performed with one-way ANOVA with Tukey's post hoc test. **p < 0.01, ***p < 0.001.

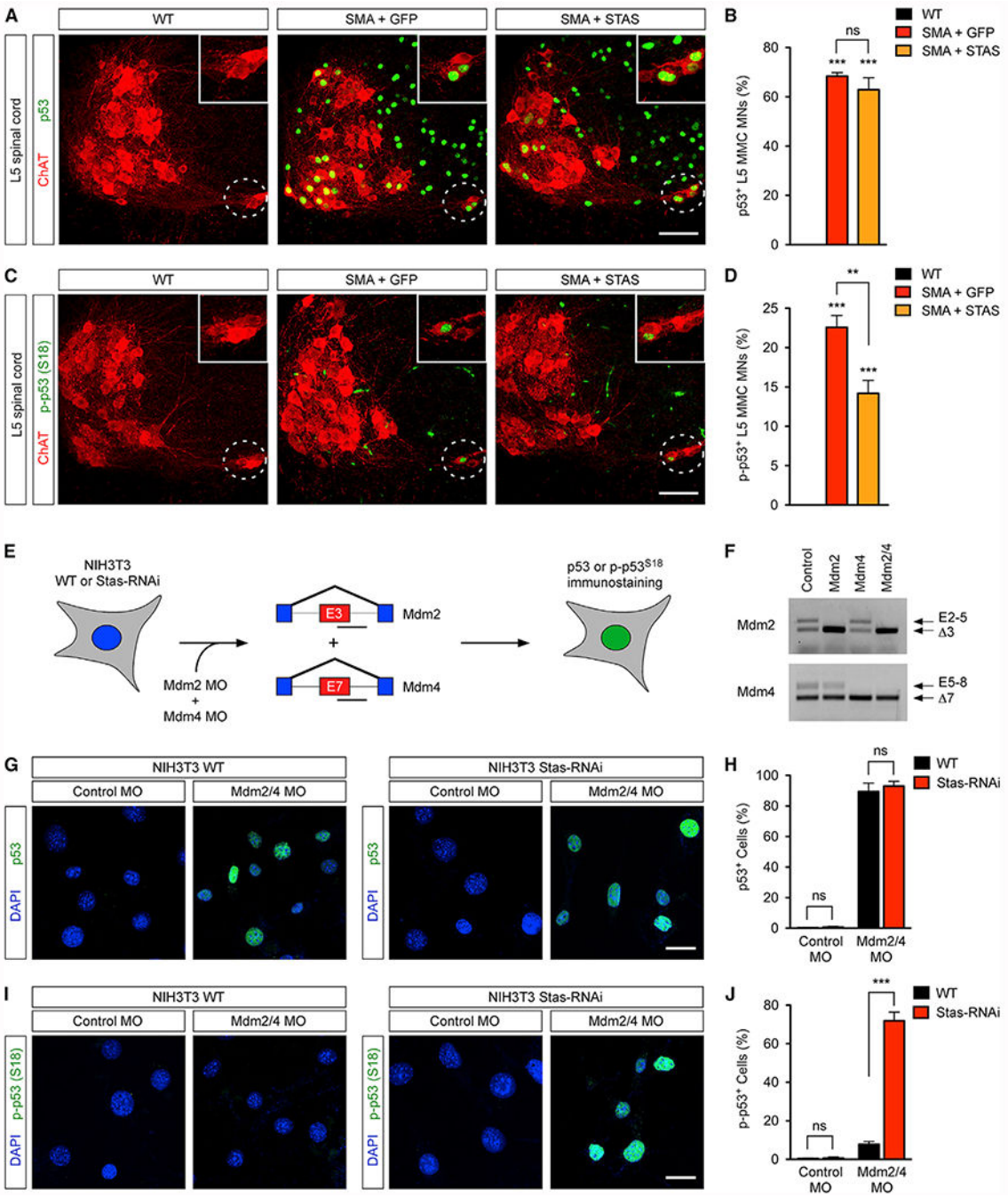

Figure 4. AAV9-STAS Decreases p53^{S18} Phosphorylation in Vulnerable SMA Motor Neurons and Stasimon Deficiency Is Sufficient to Induce p53^{S18} Phosphorylation in NIH 3T3 Cells

(A) ChAT (red) and p53 (green) immunostaining of L5 spinal cords from uninjected WT mice and SMA mice injected with AAV9-GFP or AAV9-STAS at P11. L5 MMC motor neurons are indicated by dotted circles and magnified in the insets. Scale bar: 100 μm.

(B) Percentage of p53^{+} L5 MMC motor neurons in the same groups as in (A). Data represent means and SEM from WT (n = 5), SMA+AAV9-GFP (n = 5), and SMA+AAV9-STAS (n = 5). Statistics were performed with one-way ANOVA with Tukey's post hoc test. ***p < 0.001; ns, not significant.

(C) ChAT (red) and p-p53^{S18} (green) immunostaining of L5 spinal cords from the same groups as in (A). L5MMC motor neurons are indicated by dotted circles and magnified in the insets. Scale bar: 100 μm.

(D) Percentage of p-p53^{S18+} L5 MMC motor neurons in the same groups as in (A). Data represent means and SEM from WT (n = 4), SMA+AAV9-GFP (n = 5), and SMA+AAV9-STAS (n = 6). Statistics were performed with one-way ANOVA with Tukey's post hoc test. **p < 0.01, ***p < 0.001.

(E) Schematic of the experimental design. NIH 3T3 cells (WT or Stas$_{RNAi}$) were treated with either control MOs or with splice-switching antisense MOs targeting the 5′ splice sites of Mdm2 exon 3 and Mdm4 exon 7. Nuclear accumulation of p53 and p-p53^{S18} was then assessed by immunofluorescence analysis.

(F) RT-PCR analysis of Mdm2 and Mdm4 alternative splicing in NIH 3T3 cells treated with control MOs as well as Mdm2 and Mdm4 MOs either alone or in combination.

(G) Immunofluorescence analysis of total p53 (green) in WT and Stas$_{RNAi}$ NIH 3T3 cells treated with the indicated MOs. Nuclei were counterstained with DAPI (blue). Scale bar: 25 μm.

(H) Percentage of p53^{+} NIH 3T3 cells from the same treatment groups as in (G). Data represent means and SEM (n ≥ 3). Statistics were performed with two-tailed unpaired Student's t test. ns, not significant.

(I) Immunofluorescence analysis of p-p53^{S18} (green) in WT and Stas$_{RNAi}$ NIH 3T3 cells treated with the indicated MOs. Nuclei were counterstained with DAPI (blue). Scale bar: 25 μm.

(J) Percentage of p-p53^{S18+} NIH 3T3 cells from the same treatment groups as in (I). Data represent means and SEM (n ≥ 3). Statistics were performed with two-tailed unpaired Student's t test. ***p < 0.001; ns, not significant.

See also Figure S3.

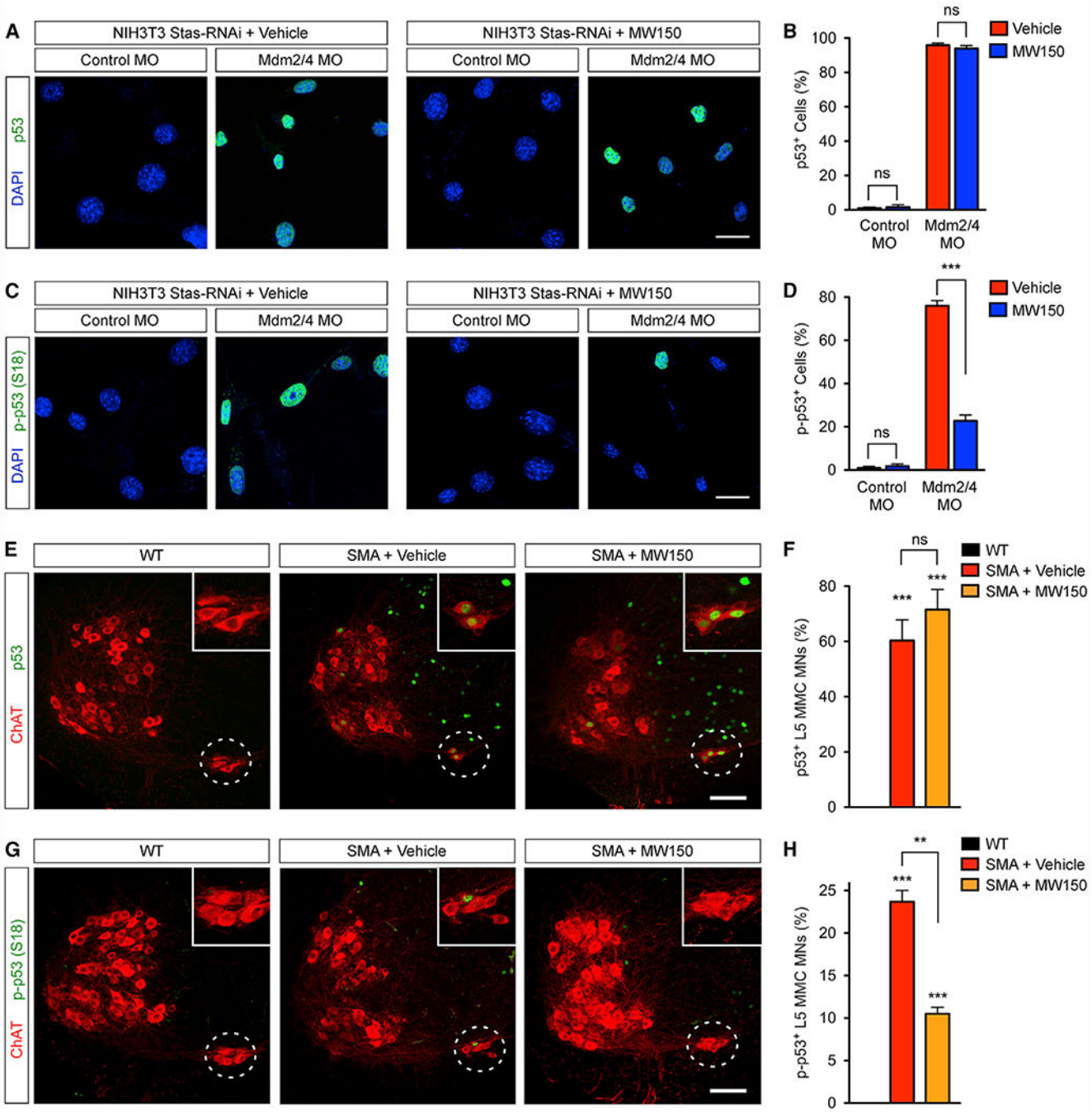

Figure 5. Stasimon-Dependent p53^{S18} Phosphorylation Is Mediated by p38α MAPK

(A) Immunofluorescence analysis of total p53 (green) in NIH 3T3-Stas$_{RNAi}$ cells treated with either vehicle or MW150 and the indicated MOs. Nuclei were counterstained with DAPI (blue). Scale bar: 25 μm.

(B) Percentage of p53^{+} NIH 3T3-Stas$_{RNAi}$ cells from the same treatment groups as in (A). Data represent means and SEM (n = 3). Statistics were performed with two-tailed unpaired Student's t test. ns, not significant.

(C) Immunofluorescence analysis of p-p53^{S18} (green) in NIH 3T3-Stas$_{RNAi}$ cells treated with either vehicle or MW150 and the indicated MOs. Nuclei were counterstained with DAPI (blue). Scale bar: 25 μm.

(D) Percentage of p-p53^{S18+} NIH 3T3-Stas$_{RNAi}$ cells from the same treatment groups as in (C). Data represent means and SEM (n = 3). Statistics were performed with two-tailed unpaired Student's t test. ***p < 0.001; ns, not significant.

(E) ChAT (red) and p53 (green) immunostaining of P11 L5 spinal cords from uninjected WT mice and SMA mice treated daily with either saline or MW150 (5 mg/kg). L5 MMC motor neurons are indicated by dotted circles and magnified in the insets. Scale bar: 100 μm.

(F) Percentage of p53^{+} L5 MMC motor neurons in the same groups as in (E). Data represent means and SEM from WT (n = 4), SMA+Vehicle (n = 4), and SMA+MW150 (n = 4). Statistics were performed with one-way ANOVA with Tukey's post hoc test. ***p < 0.001; ns, not significant.

(G) ChAT (red) and p-p53^{S18} (green) immunostaining of P11 L5 spinal cords from uninjected WT mice and SMA mice treated daily with either saline or MW150 (5 mg/kg). L5 MMC motor neurons are indicated by dotted circles and magnified in the insets. Scale bar: 100 μm.

(H) Percentage of p-p53^{S18+} L5 MMC motor neurons in the same groups as in (G). Data represent means and SEM from WT (n = 4), SMA+Vehicle (n = 4), and SMA+MW150 (n = 4). Statistics were performed with one-way ANOVA with Tukey's post hoc test. **p < 0.01, ***p < 0.001.

See also Figure S4.

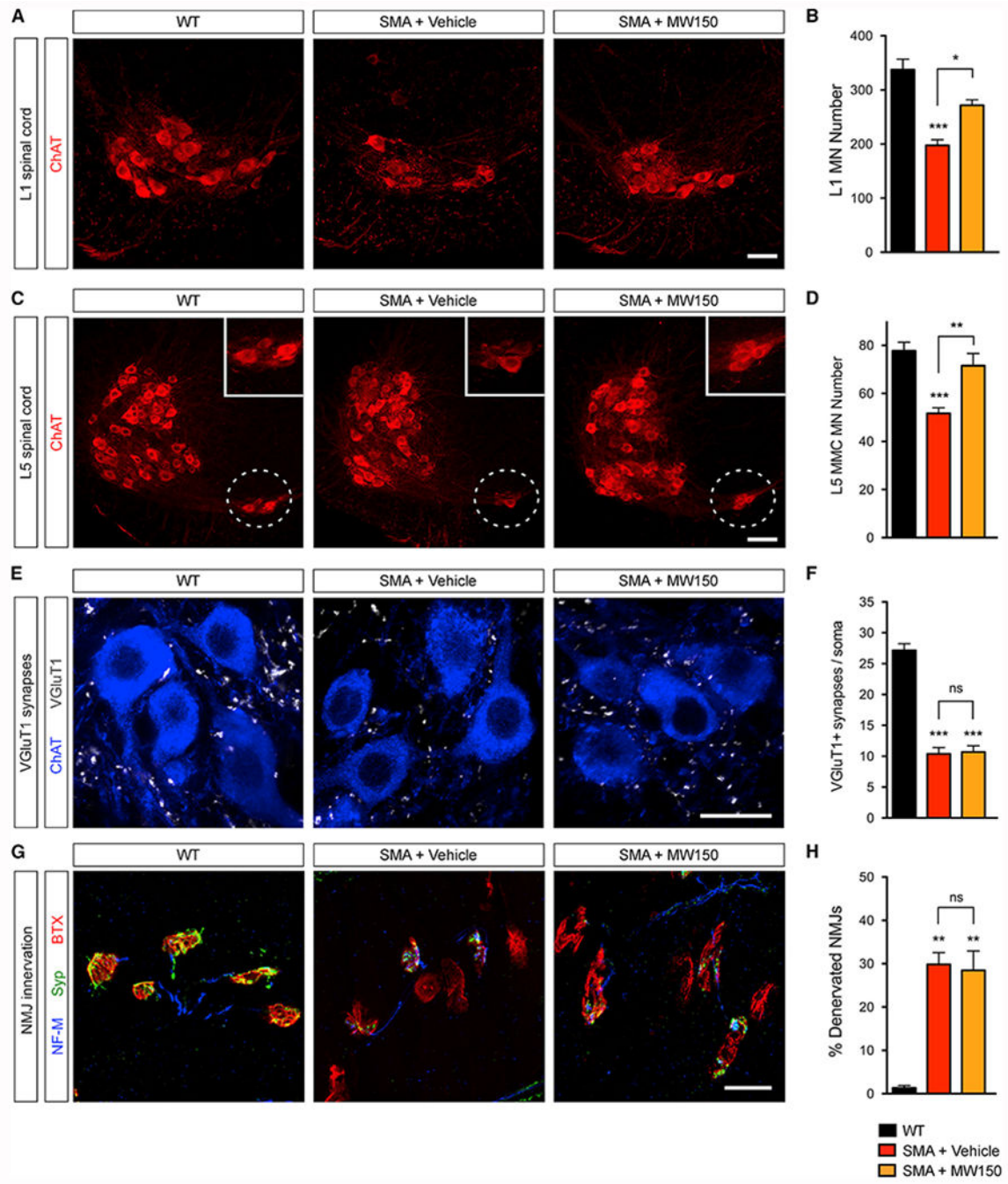

Figure 6. Treatment with the p38α MAPK Inhibitor MW150 Prevents Degeneration of SMA Motor Neurons

(A) ChAT immunostaining of P11 L1 spinal cords from uninjected WT mice and SMA mice treated daily with either saline or MW150 (5 mg/kg). Scale bar: 50 μm.

(B) Total number of L1 motor neurons in the same groups as in (A) at P11. Data represent means and SEM from WT (n = 6), SMA+Vehicle (n = 5), and SMA+MW150 (n = 3). Statistics were performed with one-way ANOVA with Tukey's post hoc test. **p < 0.01, ***p < 0.001.

(C) ChAT immunostaining of P11 L5 spinal cords from the same groups as in (A). L5 MMC motor neurons are indicated by dotted circles and magnified in the insets. Scale bar: 125 μm.
(D) Total number of L5 MMC motor neurons in the same groups as in (A) at P11. Data represent means and SEM from WT (n = 6), SMA+Vehicle (n = 6), and SMA+MW150 (n = 5). Statistics were performed with one-way ANOVA with Tukey's post hoc test. **p < 0.01, ***p < 0.001.
(E) Immunostaining of $VGluT1^+$ synapses (gray) and $ChAT^+$ motor neurons (blue) in P11 L1 spinal cords from uninjected WT mice and SMA mice treated daily with either saline or MW150 (5 mg/kg). Scale bar: 20 μm.
(F) Number of $VGluT1^+$ synapses on the somata of L1 motor neurons from the same groups as in (E) at P11. Data represent means and SEM from WT (n = 39), SMA+Vehicle (n = 39), and SMA+MW150 (n = 36). Statistics were performed with one-way ANOVA with Tukey's post hoc test. ***p < 0.001; ns, not significant.
(G) NMJ staining with bungarotoxin (BTX, red), Synaptophysin (Syp, green), and Neurofilament M (NF-M, blue) of P11 QL muscles from uninjected WT mice and SMA mice treated daily with either saline or MW150 (5 mg/kg). Scale bar: 25 μm.
(H) Percentage of fully denervated NMJs in the QL muscle from the same groups as in (G) at P11. Data represent means and SEM (n = 3). Statistics were performed with one-way ANOVA with Tukey's post hoc test. **p < 0.01; ns, not significant.

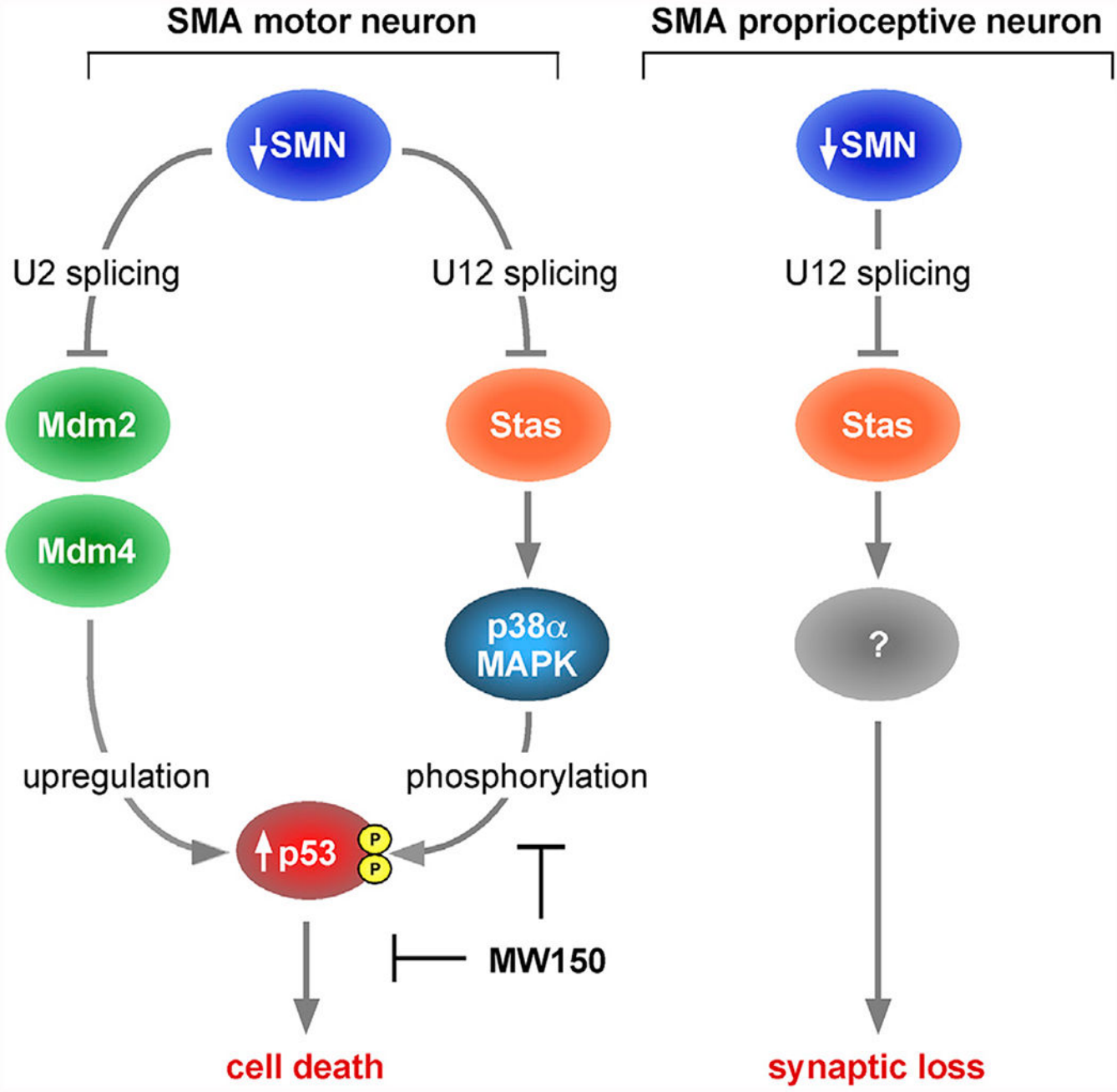

Figure 7. Dual Contribution of Stasimon to Sensory-Motor Circuit Pathology in SMA

Schematic of the role of Stasimon in the degeneration of motor neurons and the loss of proprioceptive synapses in SMA (see text for further details).

KEY RESOURCES TABLE

REAGENT or RESOURCE	SOURCE	IDENTIFIER
Antibodies		
SMN (clone 8)	BD Transd Lab	Cat#610646; RRID:AB_397973
GFP	Sigma	Cat#G1544; RRID:AB_439690
p62	MBL	Cat#PM045; RRID:AB_1279301
LC3B	Novus	Cat#NB600-1384; RRID:AB_669581
Actin	Proteintech	Cat#66009; RRID:AB_2687938
Gapdh	Millipore	Cat#MAB374; RRID:AB_2107445
Tubulin (DM1A)	Sigma	Cat#T9026 RRID:AB_477593
p38 MAPK	Cell Signaling	Cat#8690; RRID:AB_10999090
p-p38 MAPK	Cell Signaling	Cat#4511; RRID:AB_2139682
p53	Leica Novocastra	Cat#NCL-p53-CM5p; RRID:AB_563933
p-p53^{S15}	Cell Signaling	Cat#9284 (Lots: 12, 15)
Parvalbumin	Covance	custom made
VGluT1	Covance	custom made
Synaptophysin	Synaptic Systems	Cat#101-004; RRID:AB_1210382
NF-M	Millipore	Cat#AB1987; RRID:AB_91201
ChAT	Millipore	Cat#AB144; RRID:AB_90650
Bungarotoxin	Invitrogen	Cat#T1175; RRID:AB_2313931
DAPI	Molecular Probes	Cat#D3571; RRID:AB_2307445
488 Anti-rabbit	Jackson	711-545-152; RRID:AB_2313584
488 Anti-goat	Jackson	705-545-147; RRID:AB_2336933
488 Anti-chicken	Jackson	703-545-155; RRID:AB_2340375
Cy3 Anti-rabbit	Jackson	711-165-152; RRID:AB_2307443
Cy3 Anti-mouse	Jackson	715-165-150; RRID:AB_2340813
Cy3 Anti-goat	Jackson	705-165-147; RRID:AB_2307351
Cy5 Anti-goat	Jackson	705-175-147; RRID:AB_2340415
Cy5 Anti-guinea pig	Jackson	706-175-148; RRID:AB_2340462
HRP Anti-mouse	Jackson	115-035-044; RRID:AB_2338503
HRP Anti-rabbit	Jackson	111-035-003; RRID:AB_2313567
Chemicals, Peptides, and Recombinant Proteins		
Puromycin dihydrochloride	Sigma	P8833
Bafilomycin A1	Alfa Aesar	J67193XF
MW150	Roy et al., 2019	CAS 1628502-91-9
Critical Commercial Assays		
ViraPower Lentiviral Packaging Mix	Invitrogen	K497500
RevertAid RT Reverse Transcription Kit	Thermo Fisher Scientific	Cat#K1691
Experimental Models: Cell Lines		

REAGENT or RESOURCE	SOURCE	IDENTIFIER
Mouse: NIH 3T3-$Stas_{RNAi}$	This paper	N/A
Experimental Models: Organisms/Strains		
Mouse: FVB.Cg-Tg(SMN2*delta7)4299Ahmb Tg(SMN2)89Ahmb Smn1tm1Msd/J	The Jackson Laboratory	JAX:005025; RRID:IMSR_JAX:005025
Mouse: B6;129S6-$Chat^{tm2(cre)Lowl}$/J *Mus musculus*	The Jackson Laboratory	JAX:006410; RRID:IMSR_JAX:006410
Mouse: B6;129P2-$Pvalb^{tm1(cre)Arbr}$/J	The Jackson Laboratory	JAX:008069; RRID:IMSR_JAX:008069
Mouse:$Grm7^{Tg(SMN2)89Ahmb}$ $Smn1^{tm3(SMN2/Smn1)Mrph}$ Tg(SMN2*delta7)4299Ahmb/J	The Jackson Laboratory	JAX:007951; RRID:IMSR_JAX:007951
Oligonucleotides		
RT-qPCR primers for Stas mRNA, see Table S1	Lotti et al., 2012	N/A
RT-qPCR primers for Stas Aber mRNA, see Table S1	Lotti et al., 2012	N/A
RT-qPCR primers for H1c pre-mRNA, see Table S1	Tisdale et al., 2013	N/A
RT-qPCR primers for Cdkn1a mRNA, see Table S1	Ruggiu et al., 2012	N/A
RT-qPCR primers for Gapdh mRNA, see Table S1	Ruggiu et al., 2012	N/A
RT-qPCR primers for SMN2 FL mRNA, see Table S1	Ruggiu et al., 2012	N/A
RT-qPCR primers for Chodl mRNA, see Table S1	Van Alstyne et al., 2018a	N/A
RT-qPCR primers for STAS mRNA, see Table S1	This paper	N/A
RT-qPCR primers for GFP mRNA, see Table S1	This paper	N/A
RT-PCR primers for Mdm2 mRNA (E2-5), see Table S1	Van Alstyne et al., 2018a	N/A
RT-PCR primers for Mdm4 mRNA (E5-8), see Table S1	Van Alstyne et al., 2018a	N/A
PCR primers for genotyping mouse Smn, see Table S1	Simon et al., 2017	N/A
PCR primers for genotyping ChAT-Cre, see Table S1	Fletcher et al., 2017	N/A
PCR primers for genotyping PV-Cre, see Table S1	Fletcher et al., 2017	N/A
qPCR primers for AAV titration, see Table S1	This paper	N/A
Antisense morpholino oligonucleotides, see Table S1	Gene Tools	N/A
Stasimon shRNA targeting sequence: GGAAGACCCGTTGTATACA	This paper	N/A
Recombinant DNA		
dsAAV-CB-GFP	This paper	N/A
dsAAV-CB-STAS	This paper	N/A
dsAAV-CB-SMN	This paper	N/A
p.Lenti.puro/$Stas_{RNAi}$	This paper	N/A
pSUPERIOR.puro	OligoEngine	Cat#VEC-IND-0006
pRRL.SIN.cPPT.PGK-GFP.WPRE	Addgene	Plasmid 12252
Software and Algorithms		
LAS X	Leica	N/A
Prism 6	GraphPad	N/A